The Company of **Biologists**

RESEARCH ARTICLE

Mitochondrial antiviral-signalling protein is a client of the BAG6 protein quality control complex

Peristera Roboti[1],*, Craig Lawless[2] and Stephen High[1],*

ABSTRACT

The heterotrimeric BAG6 complex coordinates the direct handover of newly synthesised tail-anchored (TA) membrane proteins from an SGTA-bound preloading complex to the endoplasmic reticulum (ER) delivery component TRC40. In contrast, defective precursors, including aberrant TA proteins, form a stable complex with this cytosolic protein quality control factor, enabling such clients to be either productively re-routed or selectively degraded. We identify the mitochondrial antiviral-signalling protein (MAVS) as an endogenous TA client of both SGTA and the BAG6 complex. Our data suggest that the BAG6 complex binds to a cytosolic pool of MAVS before its misinsertion into the ER membrane, from where it can subsequently be removed via ATP13A1-mediated dislocation. This BAG6-associated fraction of MAVS is dynamic and responds to the activation of an innate immune response, suggesting that BAG6 may modulate the pool of MAVS that is available for coordinating the cellular response to viral infection.

KEY WORDS: BioID2, ER membrane complex, Protein targeting, SGTA, Tail-anchored proteins

INTRODUCTION

The endoplasmic reticulum (ER) is a major site of membrane protein synthesis, typically involving the targeting of nascent polypeptide chains to the ER by virtue of hydrophobic targeting signals, such as transmembrane domains (TMDs) or cleavable N-terminal signal peptides (Cross et al., 2009). In eukaryotes, many such targeting signals are bound by the cytosolic signal recognition particle (SRP) as they emerge from the ribosomal exit tunnel; thereby enabling their co-translational delivery to the ER for subsequent membrane insertion (Cross et al., 2009; O'Keefe et al., 2021a,b). In addition to such well-characterised co-translational pathways (O'Keefe et al., 2021a), several post-translational routes for the delivery of completed membrane proteins to the ER have been described (Farkas and Bohnsack, 2021; Hegde and Keenan, 2021). Furthermore, recent studies have revealed that, in addition to

supplying the compartments of the secretory pathway and plasma membrane with newly synthesised membrane proteins, the ER may also act as a staging post for membrane proteins en route to mitochondria. Hence, membrane proteins that initially mislocalise to the ER may be redirected to mitochondria via a mechanism termed ER-SURF (Koch et al., 2021).

Tail-anchored (TA) membrane proteins are characterised by the presence of a single TMD at their extreme C-terminus (Kutay et al., 1993), which necessitates their post-translational delivery to the appropriate subcellular organelle (Farkas and Bohnsack, 2021; Johnson et al., 2013). Although most TA proteins are inserted into the ER membrane, a smaller group is delivered to the mitochondrial outer membrane (MOM) (Costello et al., 2017). Although multiple redundant pathways have been identified, many mammalian TA proteins are delivered to the ER via the TMD recognition complex (TRC) targeting pathway (Casson et al., 2017; Farkas and Bohnsack, 2021; Hegde and Keenan, 2021). Here, SGTA captures TA clients shortly after their TMDs emerge from the ribosome to form a so-called pre-targeting complex (Farkas and Bohnsack, 2021; Leznicki and High, 2020). Subsequently, the binding of SGTA to the heterotrimeric Bag6–Ubl4A–TRC35 (hereafter BAG6) complex enables TA proteins to be handed off to the ER targeting factor TRC40 (TRC35 and TRC40 are also known as GET4 and GET3, respectively) (Farkas and Bohnsack, 2021). Once bound to TRC40, TA proteins are delivered to the ER by binding to the WRB–CAML complex (WRB is also known as GET1, and CAML as CAMLG or GET2), which acts as both a membrane receptor and insertase (McDowell et al., 2020). In comparison to our detailed understanding of TA protein biogenesis at the ER (Casson et al., 2017; Farkas and Bohnsack, 2021; Hegde and Keenan, 2021), the components and mechanisms responsible for TA protein insertion into other organellar membranes are less well-defined (Farkas and Bohnsack, 2021). One suggestion is that the membrane lipid composition may be an important factor in the selective insertion of TA proteins into the MOM (Brambillasca et al., 2005; Krumpe et al., 2012), whereas in yeast, Pex19p has been implicated in the integration of certain TA proteins at both the MOM and peroxisomes (Cichocki et al., 2018; Mayerhofer, 2016).

SGTA functions as a homodimeric co-chaperone comprised of three functional domains (see also Fig. 1A). The N-terminal region acts as a homodimerisation module that, once assembled, enables the SGTA dimer to bind either the Ubl4A or Bag6 subunits of the BAG6 complex via their respective N-terminal ubiquitin-like (UBL) domains (Roberts et al., 2015). The central tetratricopeptide repeat (TPR) domain of SGTA interacts with cytosolic heat-shock proteins and the proteasomal subunit ADRM1 (the human form of Rpn13) (Roberts et al., 2015). The C-terminal methionine-rich domain of SGTA binds hydrophobic TMDs (Liou and Wang, 2005). Its flexibility and dimeric nature are suggested to facilitate the shielding of hydrophobic TA regions and enable conformational changes that mediate downstream interactions (Lin et al., 2021; Martínez-Lumbreras et al., 2018).

[1]Division of Molecular and Cellular Function, School of Biological Sciences, Faculty of Biology, Medicine and Health, The University of Manchester, Manchester M13 9PT, UK. [2]Wellcome Trust Centre for Cell-Matrix Research, School of Biological Sciences, Faculty of Biology, Medicine and Health, The University of Manchester, Manchester M13 9PT, UK.

*Authors for correspondence (peristera.roboti@manchester.ac.uk; stephen.high@manchester.ac.uk)

P.R., 0000-0002-3360-9088; C.L., 0000-0002-8240-3430; S.H., 0000-0002-4532-8152

Journal of Cell Science
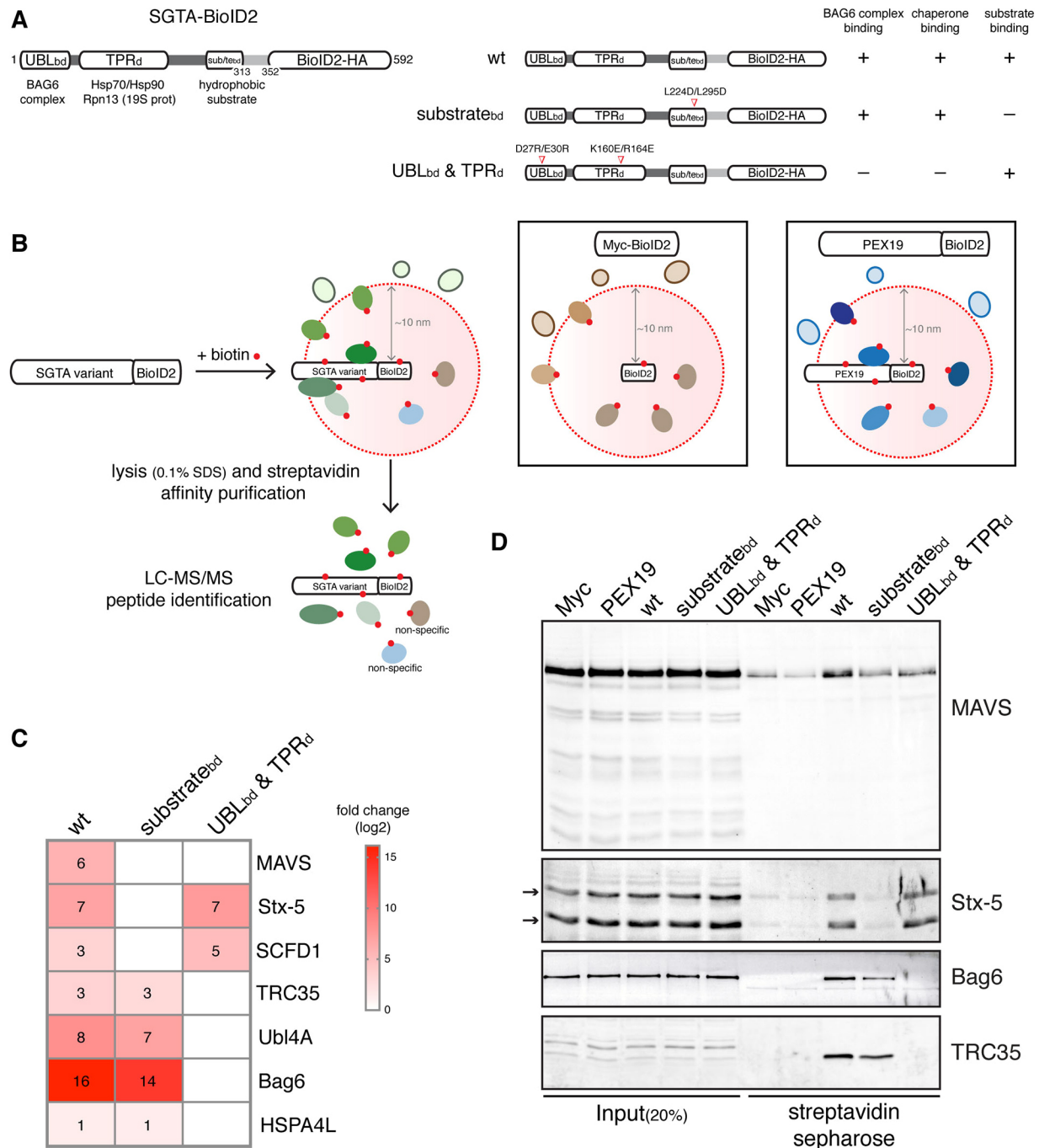
Fig. 1. MAVS is a high-confidence proximal interactor of SGTA. (A) Left, schematic of human SGTA–BioID2–HA displaying its protein–protein interaction modules. UBLbd, N-terminal domain that binds to the ubiquitin-like (UBL) domains of Ubl4A and Bag6; TPRd, central tetratricopeptide repeat (TPR) domain that interacts with heat-shock proteins; substratebd (sub/tebd), C-terminal domain that contains the hydrophobic substrate-binding site. Right, schematics of the SGTA–BioID2 mutants and respective disrupted interactions. Mutated amino acids are indicated. (B) Scheme for the BioID2-mediated proximity labelling and identification of SGTA substrates and cofactors using SGTA KO cells (see Fig. S1) transiently expressing wild-type (wt) SGTA-BioID2 or mutant variants shown in A. Cells expressing Myc–BioID2 or PEX19–BioID2 serve as two independent controls to exclude non-specific interactors. (C) Heat map representing log2-transformed fold changes in the protein intensities of significant (BFDR<0.05) wild-type (wt)/mutant SGTA-specific preys relative to both the Myc–BioID2 and PEX19–BioID2 controls. Individual rounded values are depicted in the heat map. A non-significant prey is shown as a white box (three biological replicates; see Tables S1–S3 for list of all proteins detected). (D) Validation of selected SGTA-associated candidates from C by immunoblotting. SGTA KO cells expressing the indicated BioID2-tagged baits were treated with biotin for 8 h and lysed with RIPA buffer. The resulting extracts were subjected to affinity purification with streptavidin beads and the bound material eluted using a biotin-containing buffer. The input and eluted material were analysed by immunoblotting for the indicated endogenous proteins. Stx-5 can be observed as two bands (indicated by arrows) corresponding to two isoforms, a 42 kDa-ER and a 35 kDa-Golgi isoform that result from an alternative initiation of translation (Coy-Vergara et al., 2019). Blots representative of three independent biological replicates.

The high-affinity binding of SGTA to Ubl4A subunit of the BAG6 complex facilitates the prompt and privileged transfer of TA protein clients from SGTA directly to TRC40 (Mock et al., 2015; Shao et al., 2017). In contrast, the lower affinity interaction between SGTA and the Bag6 subunit (Krysztofinska et al., 2016) enables mislocalised or defective hydrophobic precursor proteins including

aberrant TA proteins [hereafter termed mislocalised proteins (MLPs)] to be passed on from SGTA to the poorly characterised central region of the Bag6 subunit (Leznicki et al., 2013). The capacity of the BAG6 complex to recruit specialised E3 ligases facilitates the subsequent ubiquitylation and proteasomal degradation of such MLP clients (Hessa et al., 2011; Rodrigo-Brenni et al., 2014; Shao et al., 2017; Suzuki and Kawahara, 2016; Wunderley et al., 2014; Yamamoto et al., 2017). Interestingly, SGTA can antagonise this BAG6-dependent polyubiquitylation, perhaps increasing the window of opportunity for TA protein clients to access a productive outcome (Casson et al., 2016; Leznicki and High, 2012).

Although cells or tissues that lack a functional TRC pathway show substrate-specific defects in the ER targeting and membrane insertion of essential TA proteins, they remain viable (Casson et al., 2017; Jonikas et al., 2009; Norlin et al., 2016; Pfaff et al., 2016; Rivera-Monroy et al., 2016; Schuldiner et al., 2008; Vogl et al., 2016), consistent with the presence of one or more alternative pathways for TA protein biogenesis at the ER (Casson et al., 2017; Hassdenteufel et al., 2017). Likewise, at the ER membrane, in addition to the WRB–CAML-dependent integration of TA proteins delivered via TRC40 (McDowell et al., 2020), the ER membrane protein complex (EMC) acts as an ER membrane insertase for TA proteins with moderately hydrophobic TMDs that cannot efficiently exploit the TRC40 pathway (Guna et al., 2018).

Here, we use BioID2-based proximity labelling to identify the mitochondrial antiviral-signalling protein (MAVS) as an endogenous TA client of SGTA. MAVS has been detected at the MOM, peroxisomes and mitochondria-associated ER membrane subdomains (mitochondria-associated membranes; MAMs) and is implicated in innate immune signalling at each of these locations (Thoresen et al., 2021; Vazquez and Horner, 2015). MAVS is also prone to being 'mislocalised' to the ER membrane, from where it can be removed by the P5A-type ATPase ATP13A1 (McKenna et al., 2020). Like other TA proteins, we find that MAVS can be handed off from SGTA to the BAG6 quality control complex, which is stably associated with a pool of cytosolic MAVS. To further explore the origin of this BAG6-bound pool of MAVS, we manipulated its ER-mislocalised form by knocking down its likely membrane insertase, the EMC, and dislocase, the ATP13A1 protein. Our resulting data suggest a model whereby cytosolic MAVS binds the BAG6 complex before misinsertion into the ER membrane. BAG6-bound MAVS responds to the activation of an innate immune response, and we speculate that BAG6 might modulate MAVS activity, perhaps by contributing to the recently identified ER-SURF pathway and/or supplying MAVS to MAMs.

RESULTS
BioID2 screening for proximal SGTA interactors
To identify clients and cofactors of SGTA, we used the promiscuous biotin ligase BioID2 to label its neighbouring proteins in cultured mammalian cells (Kim et al., 2016), reasoning this approach would be well suited to identifying relevant weak and/or transient interactions (Shao et al., 2017; Wunderley et al., 2014; Xu et al., 2012). We generated SGTA baits that carried BioID2–HA (hereafter BioID2) at the C-terminus, a position close enough to the substrate-binding domain to allow labelling (Liou and Wang, 2005; Martínez-Lumbreras et al., 2018; Wang et al., 2010). Three forms of SGTA were used; wild-type SGTA, a substrate-binding domain mutant (substrate$_{bd}$mt) that exhibits significantly reduced affinity for hydrophobic clients (Lin et al., 2021) and a combined UBL-binding and TPR domain mutant [(UBL$_{bd}$ & TPR$_d$)mt], which is

defective in its interactions with the BAG6 complex, molecular chaperones and the proteasome, but retains its ability to bind clients (Leznicki et al., 2015; Walczak et al., 2014; Xu et al., 2012) (Fig. 1A).

By comparing the profile of biotinylated proteins obtained using these three SGTA variants, we hoped to distinguish candidate substrates/clients from cofactors. In order to control for the specificity of these SGTA-proximal proteomes, we also used cells expressing either Myc-tagged BioID2 or BioID2–HA fused to PEX19, a cytosolic chaperone implicated in the biogenesis of lipid droplet proteins at the ER (Schrul and Kopito, 2016) and TA proteins at peroxisomes and mitochondria (Cichocki et al., 2018; Mayerhofer, 2016) (Fig. 1B). These various BioID2 fusions were expressed in SGTA-knockout (KO) HepG2 cells (Fig. S1A,B), thereby removing any competition with the endogenous protein. Although the TA proteins that SGTA hands over to TRC40 most likely include several SNARE proteins that are involved in vesicular trafficking (Coy-Vergara et al., 2019), global protein secretion appeared unaffected in the SGTA KO cell line (Fig. S1C).

In preliminary experiments, BioID2-tagged baits were transiently expressed in SGTA KO cells that were treated with exogenous biotin for 8 h to confirm labelling efficiency. In contrast to the smaller Myc–BioID2, which was present throughout the cell, the SGTA–BioID2 variants and PEX19–BioID2 fusion all showed a diffuse cytosolic signal by immunofluorescence microscopy, consistent with the location of biotinylated proteins that were labelled using a streptavidin-conjugated fluorescent probe (Fig. S2A). Likewise, comparable levels of self-biotinylation were seen with each of the BioID2-tagged baits (Fig. S2B), and we proceeded to analyse their respective interactomes. As proof of principle, we next examined the ability of SGTA–BioID2 to biotinylate known interacting partners by immunoblotting (Fig. S2C–E). As expected, the Bag6 protein and cytosolic Hsp90-α/β were present in the streptavidin-bound material recovered from cells expressing wild-type SGTA-BioID2 and substrate$_{bd}$mt, but were absent in the pulldown material from cells expressing (UBL$_{bd}$ & TPR$_d$)mt (Fig. S2C–E). The known TRC40 client syntaxin-5 (Stx-5) (Coy-Vergara et al., 2019; Norlin et al., 2016) was efficiently recovered from the lysate of cells expressing wild-type SGTA–BioID2, but the amount pulled down was much reduced in substrate$_{bd}$mt-expressing cells (Fig. S2C,E). We therefore conclude that we can selectively biotinylate known SGTA partners and discriminate between cofactors and substrates based on their labelling with different SGTA–BioID2 variants.

To further characterise the proximal environment of SGTA, we performed large-scale BioID2 experiments in SGTA KO HepG2 cells, identified high-confidence interactors using the significance analysis of interactome (SAINT) algorithm (Teo et al., 2014) (Fig. 1C; Fig. S3; see complete list in Tables S1–S3) and validated selected candidates by immunoblotting (Fig. 1D). Wild-type and substrate$_{bd}$mt baits confirmed the proximity of SGTA to the three subunits of the BAG6 complex, i.e. Bag6, Ubl4A and TRC35 (see Casson et al., 2016), and the Hsp70 chaperone, HSPA4L (see table S3 in Pourhaghighi et al., 2020) (Fig. 1C,D). In contrast, the TRC40 TA protein client Stx-5 (Coy-Vergara et al., 2019) and its conserved partner Sec1 family domain-containing protein 1 (SCFD1) were selectively labelled by wild-type and (UBL$_{bd}$ & TPR$_d$)mt baits (Fig. 1C,D). These results validated the data from our small-scale study, identified Stx-5 as a bona fide SGTA client, and confirmed that our approach can differentiate between cofactors and substrates.

Our BioID2 analysis suggested a selective association between wild-type SGTA and the mitochondrial TA protein MAVS (see

Fig. 1C; Fig. S3; Tables S1–S3). Furthermore, biotinylated MAVS was efficiently recovered in the streptavidin pulldown material from cells expressing wild-type SGTA, but its pulldown levels were reduced when using lysates of cells expressing both SGTA variants (Fig. 1D). The mitochondrial localisation of MAVS, together with its role in innate immunity (Thoresen et al., 2021), prompted us to study its interaction with SGTA in more detail.

MAVS is a substrate of SGTA

To confirm the findings from our BioID2 labelling, we assessed the association between endogenous SGTA and MAVS by co-immunoprecipitation using cytosol prepared from control KO HepG2 cells (Fig. 2A,B). This fraction was enriched for known cytosolic proteins including SGTA, Bag6 and tubulin, but largely depleted of integral membrane protein markers for the ER (calnexin) and mitochondria (TOM20), which were recovered in the pellet (Fig. 2A). Interestingly, ~40% of full-length MAVS was recovered in the cytosolic fraction (Fig. 2A), which is reminiscent of results in previous reports showing that a fraction of the Golgi-resident TA protein Stx-5 is recovered in the cytosol (Coy-Vergara et al., 2019). Furthermore, both of these TA proteins were co-immunoprecipitated with SGTA from this cytosolic fraction (Fig. 2B), confirming the interactions that were suggested by our BioID2 analysis (Fig. 1).

Previous *in vitro* studies have shown that SGTA binds to exposed hydrophobic TMDs (Liou and Wang, 2005), including those of TA proteins (Itakura et al., 2016; Leznicki et al., 2010), and we therefore used a pulldown assay (Leznicki and High, 2020) to investigate the interaction of MAVS with SGTA (Fig. 2C). Following *in vitro* translation of FLAG-tagged MAVS variants in the presence or absence of recombinant His-S-tag-SGTA, SGTA-bound clients were captured using cobalt resin. Radiolabelled wild-type FLAG–MAVS and a version lacking its characteristic N-terminal caspase activation and recruitment domain (ΔCARD) were both efficiently recovered with SGTA (Fig. 2C, eluates). In contrast, removal of its hydrophobic TMD (ΔTMD) prevented MAVS from forming a stable interaction with SGTA (Fig. 2C, eluates), consistent with results in previous studies of SGTA clients (Leznicki et al., 2010; Leznicki and High, 2020; Wang et al., 2010). Taken together, these results confirm that MAVS is an authentic endogenous binding partner of SGTA, and suggest that its primary mode of interaction is TMD dependent.

MAVS exhibits a robust interaction with the BAG6 complex that may be facilitated by SGTA

Previous studies have identified MAVS as a potential interacting partner of BAG6 (Antonicka et al., 2020; Li et al., 2011), which typically acts downstream of SGTA (Farkas and Bohnsack, 2021; Hegde and Keenan, 2021). We therefore extended our co-immunoprecipitation study and found that MAVS is also an endogenous client of the BAG6 protein quality control complex (Benarroch et al., 2019) (Fig. 3A; Fig. S4A,B). In contrast to MAVS, we found no evidence that a second endogenous TA protein of the MOM, OMP25 (also known as SYNJ2BP), is a potential SGTA client (Tables S1–S3) and does co-precipitate with the BAG6 complex (Fig. S4B). Hence, whereas OMP25 was previously shown to interact with SGTA and the BAG6 complex *in vitro* when its target MOM was absent (Itakura et al., 2016), our cell-based assay suggests that alternative TMD-binding factors deal with OMP25 molecules that fail to become membrane-inserted. Furthermore, unlike MAVS, we find no evidence for a substantial pool of OMP25 in the cytosol of HepG2 cells (Fig. S4B). Nevertheless, we explored

the possibility that any uninserted OMP25 may bind to the ubiquilins, which are reported to act as TMD-binding chaperones that prevent OMP25 aggregation prior to its membrane insertion or degradation (Itakura et al., 2016). However, we were unable to confirm any interaction between endogenous OMP25 and ubiquilin-2 by co-immunoprecipitation (Fig. S5A), consistent with our fractionation studies, which suggest that the majority of OMP25 is membrane inserted at steady state (Figs S4B and S5A). Likewise, we find no evidence that MAVS forms a stable complex with the ubiquilins under identical conditions to those used to recover the BAG6 complex bound to both MAVS and Stx-5 (Fig. S5B). Hence, although MAVS and OMP25 have similarly hydrophobic TMDs and basic residues at their C-termini (Fig. S4C), which are characteristic of TA proteins destined for the MOM (Costello et al., 2017; Rao et al., 2016), our data suggest that MAVS is a favoured client of the BAG6 complex.

Our next step was to evaluate whether SGTA played any role in the binding of MAVS to the BAG6 complex, consistent with its previously established role in TA protein biogenesis (Farkas and Bohnsack, 2021). Quantification of the relative amount of MAVS species that were co-immunoprecipitated with Bag6 (see Materials and Methods, Immunoblotting section) suggested a reduction in the amount of MAVS that was associated with the Bag6 protein (Fig. 3B,C). These results support previous models that propose that SGTA acts upstream of the BAG6 complex to which it hands off hydrophobic substrates en route to either the ER membrane or regulated proteasomal degradation (Casson et al., 2016; Farkas and Bohnsack, 2021; Shao et al., 2017). However, these data also show that the loss of SGTA does not preclude MAVS binding to BAG6, implying there are alternative pathways for their association (see Discussion). Collectively, these findings suggest that the BAG6 complex interacts with the mitochondrial TA protein MAVS via a mechanism that might be facilitated by SGTA, most likely acting as an upstream delivery factor.

ATP13A1 deficiency does not affect the BAG6–MAVS interaction

ATP13A1 is an ER-resident P5A-ATPase that has been implicated in the extraction of mitochondrial TA proteins including MAVS and OMP25 that can mislocalise to the ER membrane (McKenna et al., 2020). Given the ability of Bag6 and SGTA to bind membrane protein substrates that are dislocated into the cytosol via the pathways responsible for ER-associated protein degradation (ERAD) (Benarroch et al., 2019), we postulated that BAG6 may bind MAVS after its ATP13A1-mediated dislocation from the ER membrane.

To test this hypothesis, we compared the cytosolic population of MAVS recovered with BAG6 in control and ATP13A1-depleted cells, reasoning that an inhibition of ATP13A1-mediated dislocation from the ER membrane would impair any downstream interaction of MAVS with the BAG6 complex (Fig. 4A). In ATP13A1-knockdown cells (~70% reduction; Fig. 4Bi,ii), levels of both total cellular MAVS and its cytoplasmic pool showed a modest decrease (Fig. 4B), consistent with a partially redundant role for ATP13A1 in MAVS dislocation from the ER (McKenna et al., 2020). However, depletion of ATP13A1 had no significant effect on the amount of MAVS that co-immunoprecipitated with the BAG6 complex (Fig. 4C,D). These findings indicate that ATP13A1 deficiency does not compromise the BAG6-bound cohort of MAVS, arguing against the hypothesis that MAVS is handed over to the BAG6 complex via an ATP13A1-dependent mechanism.
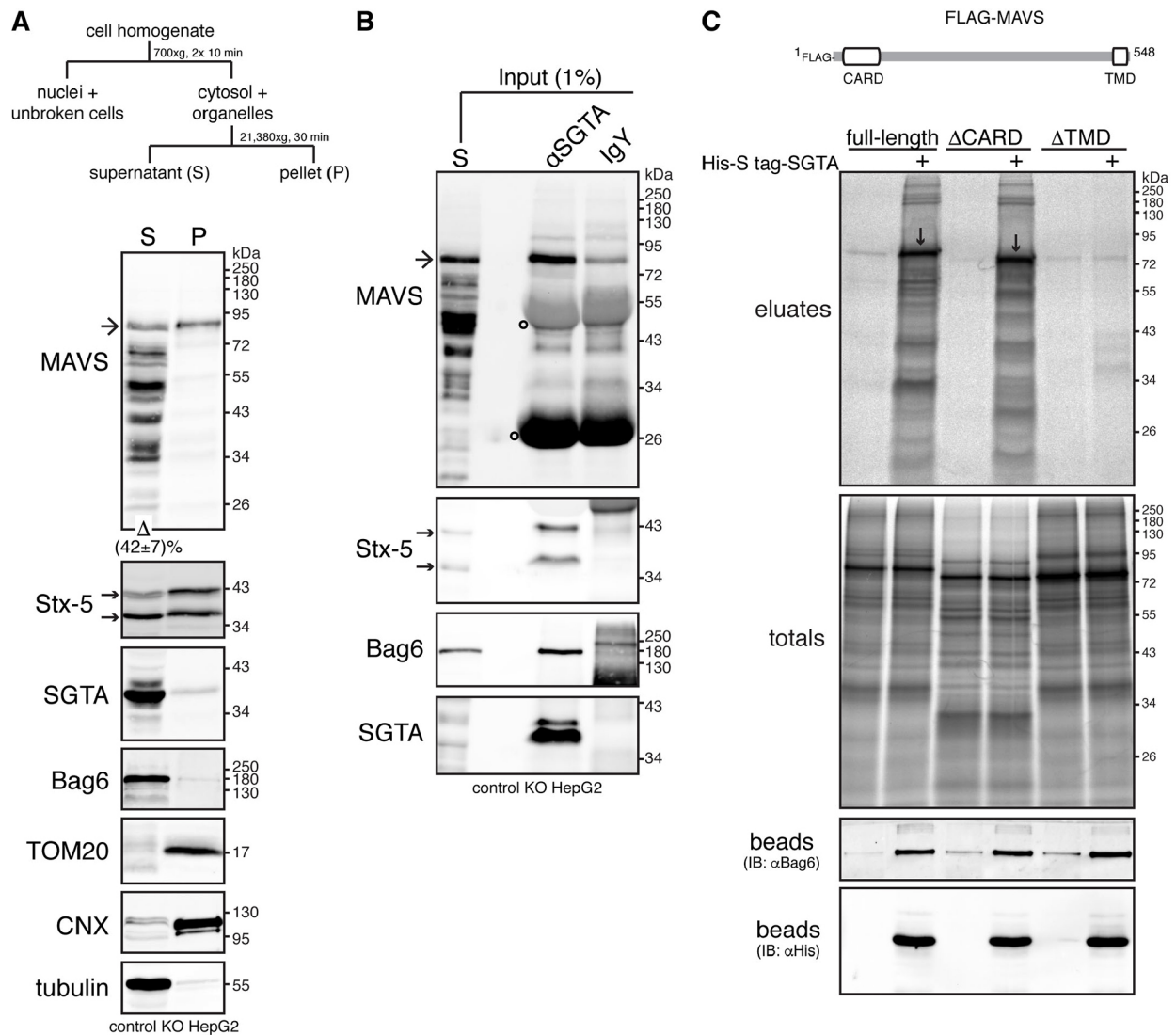
Fig. 2. SGTA interacts with MAVS. (A) A cytosolic pool of endogenous MAVS can be observed at steady-state. Top, schematic of subcellular fractionation protocol used to separate the cell homogenate into crude cytosolic supernatant (S) and membrane-associated pellet (P) fractions. Bottom, detergent-free extracts from control KO cells (see Fig. S1) were fractionated as shown above. Equivalent amounts of each fraction were analysed by immunoblotting for MAVS and various compartmental markers. Bag6, SGTA and tubulin (cytosolic markers), TOM20 (mitochondrial outer membrane marker) and calnexin (CNX, ER membrane marker) serve as fractionation controls. Note that the MAVS-specific antibody, raised against amino acids 1–135 of human MAVS, detected the ~80 kDa full-length MAVS (marked by an arrow) and multiple shorter variants that most likely represent C-terminally degraded products or processed forms of the full-length protein (see also Seth et al., 2005). Quantification of the levels of full-length MAVS recovered in the cytosolic fraction is indicated below the MAVS blot. Value represents mean±s.e.m. from three independent experiments. (B) MAVS co-immunoprecipitates with SGTA. The supernatant (S) fraction from A was subjected to immunoprecipitations with equal amounts of chicken anti-SGTA antibody (αSGTA) or chicken IgY antibody (control for non-specific binding). Input and immunoprecipitates were analysed by immunoblotting for the indicated endogenous proteins. Bag6 served as positive control for SGTA binding. In A and B, arrows next to the Stx-5 blots indicate the two Stx-5 isoforms. Open circles on MAVS blots indicate signals derived from denatured antibody heavy and light chains. Blots representative of three independent experiments. (C) In vitro translated MAVS interacts with recombinant SGTA via its transmembrane domain (TMD). Top, schematic of FLAG–MAVS displaying its N-terminal caspase activation and recruitment domain (CARD) and C-terminal TMD. Bottom, FLAG-MAVS full-length, ΔCARD or ΔTMD truncated variants were translated in vitro in the absence or presence (+) of 2 μM His-S-tag-SGTA. A 10% sample of the total translation products was subjected to denaturing immunoprecipitations with anti-FLAG antibody (totals), while the rest was incubated with HisPur cobalt resin and bound proteins were eluted using imidazole (eluates). Totals and eluates were resolved by SDS-PAGE and results visualised by phosphorimaging. Downward arrows indicate full-length and ΔCARD FLAG–MAVS selectively bound by His-S-tag-SGTA. His-S-tag-SGTA and its binding partners within rabbit reticulocyte lysate were released from the resin by incubating the beads with SDS sample buffer (beads) and samples were analysed by immunoblotting (IB). The anti-His and anti-Bag6 immunoblots indicate uniform binding of Bag6 binding-competent His-S-tag-SGTA to beads. Results shown in C are representative of two independent experiments.

EMC5 deficiency enhances BAG6–MAVS interaction

Prompted by the potential ER mislocalisation of a population of mitochondrial MAVS (McKenna et al., 2020), we next asked whether the association of MAVS with the BAG6 complex occurs before MAVS insertion into the ER membrane. Earlier work had already established that MAVS is integrated into cellular membranes via a TRC40–WRB–CAML-independent pathway (Coy-Vergara et al., 2019). We therefore focussed our attention on the EMC, which provides an alternative route for the membrane insertion of certain TA proteins (compare with Coy-Vergara et al., 2019) and shows structural homology to the CAML subunit of the TRC40-dependent membrane insertion complex
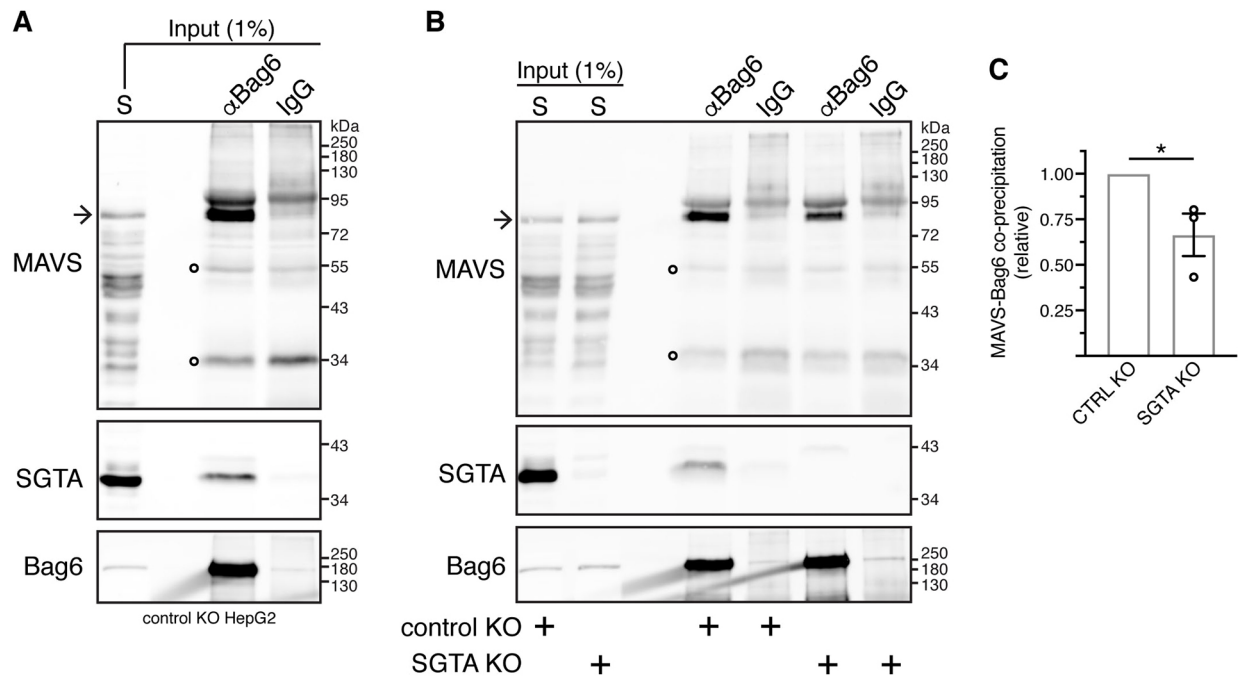
Fig. 3. Bag6 interacts with MAVS. (A) MAVS co-immunoprecipitates with Bag6. Control KO cells were fractionated as shown in Fig. 2A and the supernatant (S) fraction was subjected to immunoprecipitations with equal amounts of rabbit anti-Bag6 antibody (αBag6) or rabbit IgG antibody (control for non-specific binding). Input and immunoprecipitates were analysed by immunoblotting for the indicated endogenous proteins. SGTA served as positive control for Bag6 binding. (B) SGTA facilitates Bag6–MAVS interaction. Control KO and SGTA KO cells were fractionated as shown in Fig. 2A and the supernatant (S) fractions were subjected to immunoprecipitations with rabbit anti-Bag6 antibody (αBag6) or rabbit control IgG antibody. Inputs and immunoprecipitates were analysed by immunoblotting for the indicated endogenous proteins. SGTA served as positive control for Bag6 binding. Arrow in A and B indicates full-length MAVS. Open circles on MAVS blots indicate signals derived from denatured antibody heavy and light chains. (C) Mean±s.e.m. of MAVS levels that co-immunoprecipitate with Bag6 in control KO and SGTA KO cells for three independent experiments as in B. *$P<0.05$ (unpaired two-tailed t-test).

(McDowell et al., 2020). In this scenario, if MAVS accesses an EMC-mediated pathway for ER insertion operating downstream of BAG6, then any perturbation of this pathway could alter the pool of MAVS available to bind to BAG6 (Fig. 5A).

To explore this possibility, we compared the cytosolic population of MAVS bound to BAG6 in both control and EMC-depleted cells upon knocking down the 'core' EMC5 (also known as MMGT1) subunit (see also O'Keefe et al., 2021b). Notably, in HepG2 cells, we achieved a ~90% depletion of EMC5 accompanied by a significant reduction of two other 'core' EMC subunits, EMC1 and EMC2 (Fig. 5Bi,iii), presumably destabilising the entire EMC (see also O'Keefe et al., 2021b). Although an EMC5 knockdown did not noticeably alter the distribution of MAVS following fractionation (Fig. 5Bii,iv), the BAG6-bound pool of MAVS was increased by ~60% following EMC5 depletion when compared to control cells (Fig. 5C,D), consistent with a smaller, although non-significant, increase (~10%) in cytosolic MAVS (Fig. 5Bii,iv). These results are consistent with a model where the pool of BAG6-bound MAVS is dependent on the amount of cytosolic MAVS that is available for binding. Furthermore, since we see an effect of perturbing MAVS insertion into, but not its dislocation from, the ER membrane (compare Figs 4 and 5), we conclude that the BAG6 complex most likely captures newly synthesised MAVS before its membrane integration (see Discussion).

BAG6–MAVS interaction is modulated during MAVS-dependent innate immune signalling

MAVS plays a central role in innate immune responses to the RNA virus infection of mammalian cells, acting downstream of viral RNA receptors which, upon binding MAVS at the

MOM, trigger the formation of prion-like MAVS aggregates (Thoresen et al., 2021). These then serve as signalling platforms for the activation of interferon regulatory type 3 (IRF3) and nuclear factor κB (NF-κB) transcription factors (Thoresen et al., 2021) (Fig. S6A). Following activation, MAVS is ubiquitylated and subsequently targeted for proteasomal or lysosomal degradation, thereby diminishing downstream signalling (Ren et al., 2020).

Given the well-established role of the BAG6 complex in the quality control of hydrophobic precursor proteins that have mislocalised to the cytosol (Benarroch et al., 2019; Casson et al., 2017), we investigated the possibility that it may be involved in the regulated degradation of MAVS. To test this, we transfected control or Bag6-depleted cells with high-molecular-mass polyinosinic-polycytidylic acid [poly(I:C)], which mimics the intracellular double-stranded (ds)RNA generated during viral replication and specifically activates the MDA5 RIG-I-like receptor (also known as IFIH1) (Kato et al., 2008), and examined the activation of IRF3, a signalling pathway component acting downstream of MAVS (Fig. S6A). No obvious effects on either the phosphorylation or dimerisation of IRF3 were detected following knockdown of the Bag6 protein (Fig. S6B,C), suggesting that the BAG6 complex is not an essential component for the cellular mobilisation of a MAVS-dependent response to viral infection.

We next addressed whether the activation of MAVS-dependent signalling might modulate the cytosolic pool of MAVS that is bound to the BAG6 complex. Stimulation with poly(I:C) induced phosphorylation and dimerisation of IRF3, but had no effect on total IRF3 levels (Fig. 6A). In agreement with the previously observed downregulation of MAVS expression following virus-
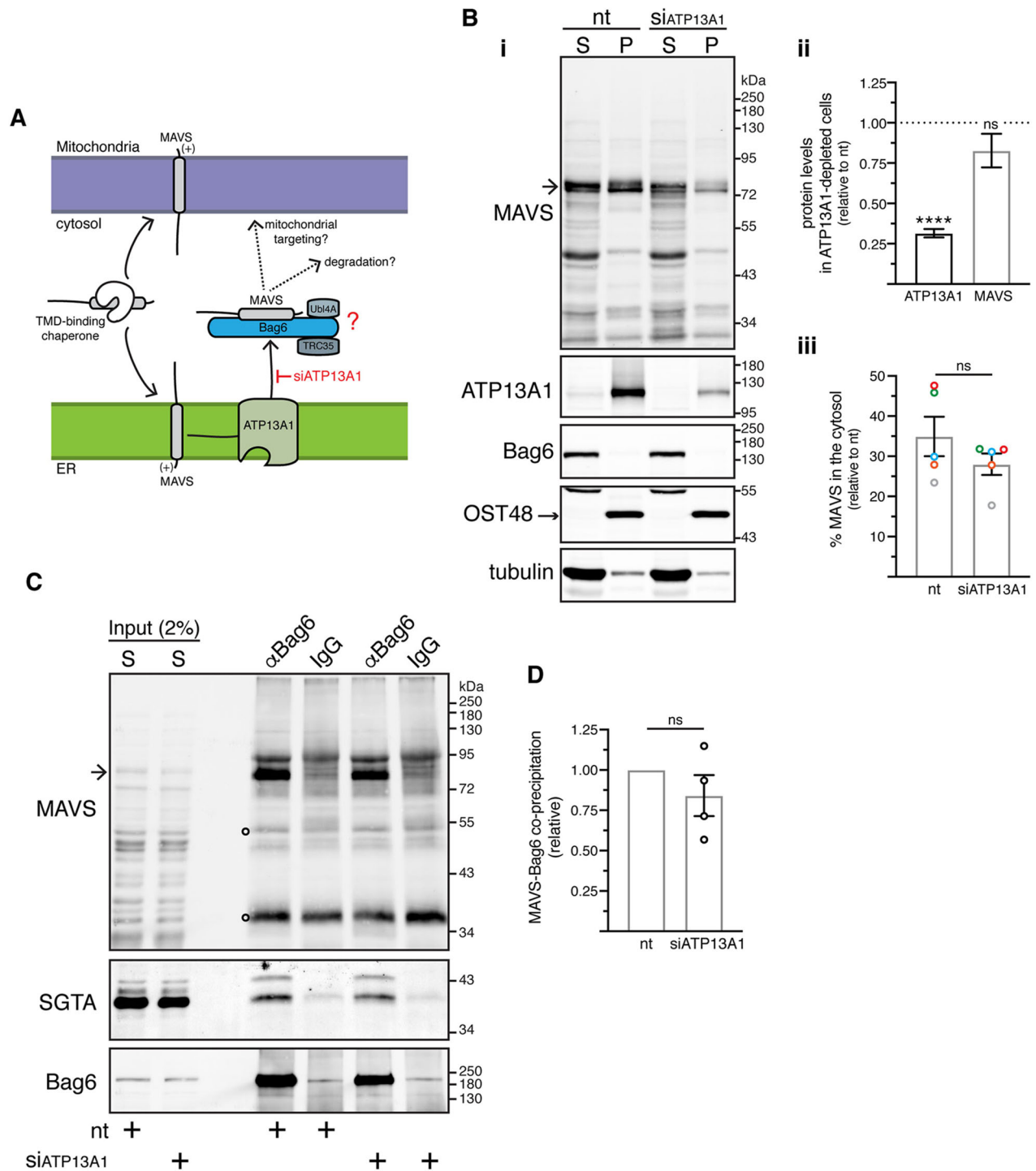
Fig. 4. ATP13A1 depletion has no visible effect on Bag6-MAVS interaction. (A) Proposed model. Bag6 recruits MAVS after its ATP13A1-mediated extraction from the ER membrane. Depleting ATP13A1 will decrease Bag6-MAVS interaction, as MAVS cannot be dislocated from the ER membrane. (B) ATP13A1 depletion does not grossly alter the levels of MAVS in the crude cytosolic supernatant fraction. (i) Control KO cells transfected with non-targeting (nt) or ATP13A1-targeting siRNAs (siATP13A1) were fractionated as shown in Fig. 2A. Equivalent amounts of supernatant (S) and pellet (P) fractions were analysed by immunoblotting for the indicated endogenous proteins. (ii) ATP13A1 and MAVS levels in siATP13A1-treated cells relative to nt siRNA-treated cells, where protein levels were set to 1. Shown are means±s.e.m. for five biological replicates as shown in Bi. ****$P<0.0001$; ns, not significant (two-tailed one-sample t-test). (iii) Mean±s.e.m. of the supernatant/total ratio of MAVS levels in siATP13A1-treated cells relative to the respective ratio in nt siRNA-treated cells for five independent experiments as in Bi. Same colour data points correspond to a single biological replicate; ns, not significant (paired two-tailed t-test). (C) ATP13A1 depletion does not affect Bag6-MAVS interaction. Supernatant (S) fractions from Bi were subjected to immunoprecipitations with rabbit anti-Bag6 antibody (αBag6) or rabbit control IgG antibody. Inputs and immunoprecipitates were analysed by immunoblotting for the indicated endogenous proteins. SGTA served as loading control as well as an internal control for equal Bag6 co-immunoprecipitation potential. Arrow in Bi and C indicates full-length MAVS. Open circles on MAVS blots indicate signals derived from denatured antibody heavy and light chains. (D) Mean±s.e.m. of MAVS levels that co-immunoprecipitate with Bag6 in siATP13A1-treated cells relative to nt siRNA-treated cells for four independent experiments as shown in C. ns, not significant (paired two-tailed t-test).
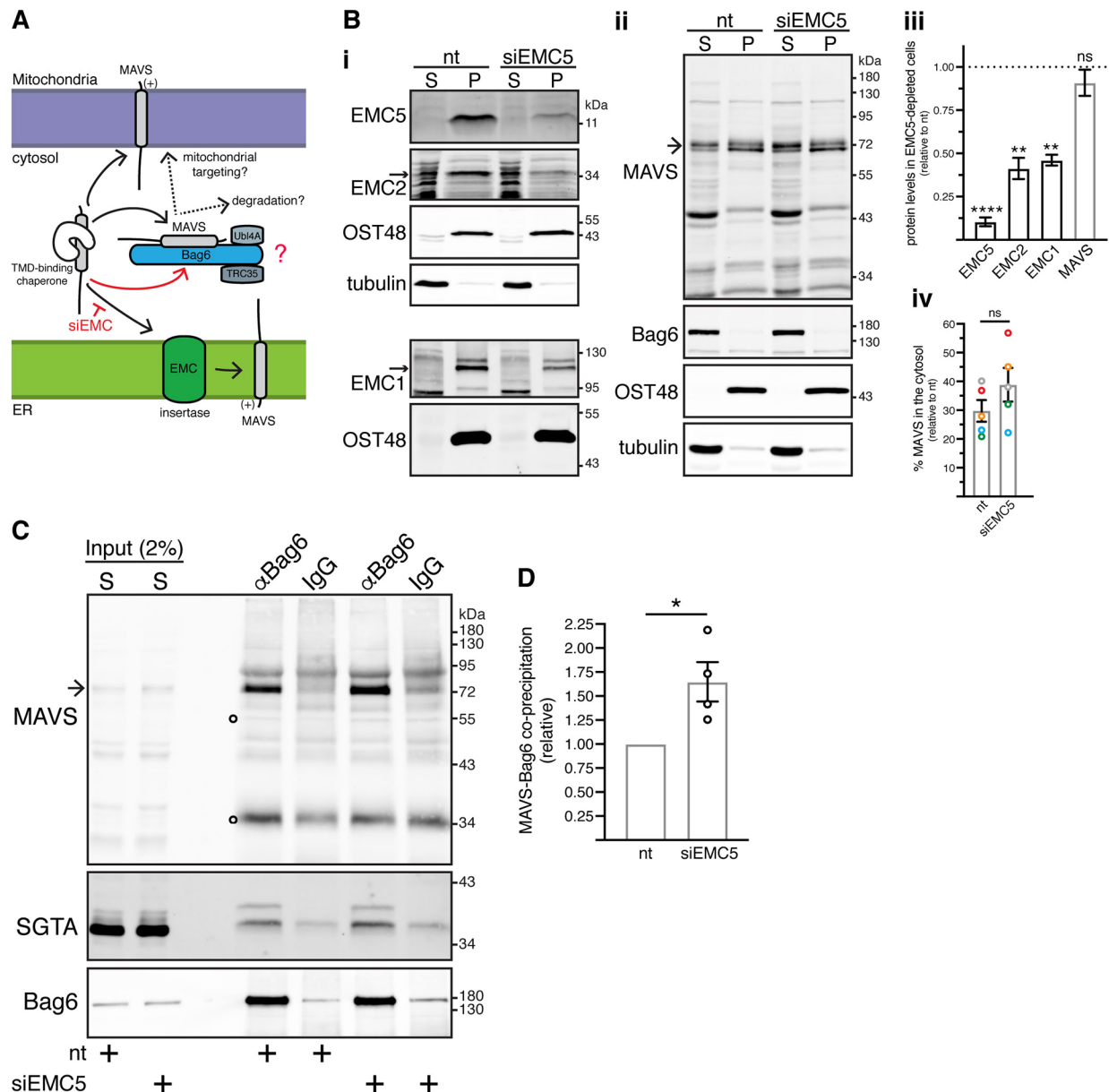
Fig. 5. EMC5 depletion enhances Bag6–MAVS interaction. (A) Proposed model. Bag6 binds MAVS before its EMC-mediated integration at the ER membrane. EMC deficiency will promote Bag6 binding to the cytosolic pool of MAVS that fails to be imported into the ER membrane. (B) EMC5 depletion does not grossly alter the levels of MAVS in the crude cytosolic supernatant fraction. (i,ii) Control KO cells transfected with non-targeting (nt) or EMC5-targeting siRNAs (siEMC5) were fractionated as shown in Fig. 2A. Equivalent amounts of supernatant (S) and pellet (P) fractions were analysed by immunoblotting for the indicated endogenous proteins. Blots resulting from the same membrane are clustered together. Tubulin and OST48 serve as loading controls for the supernatant and pellet fractions, respectively. (iii) EMC subunit and MAVS levels in siEMC5-treated cells relative to nt siRNA-treated cells, where protein levels were set to 1. Shown are means ±s.e.m. for three-five biological replicates as shown in Bi,ii. ****$P<0.0001$; **$P<0.01$; ns, not significant (one-way ANOVA with Tukey's multiple comparison tests). (iv) Mean±s.e.m. of the supernatant/total ratio of MAVS levels in siEMC5-treated cells relative to the respective ratio in nt siRNA-treated cells for five independent experiments as in Bii. Same colour data points correspond to a single biological replicate; ns, not significant (paired two-tailed t-test). (C) EMC5 depletion enhances Bag6-MAVS interaction. Supernatant (S) fractions from Bi,ii were subjected to immunoprecipitations with rabbit anti-Bag6 antibody (αBag6) or rabbit control IgG antibody. Inputs and immunoprecipitates were analysed by immunoblotting for the indicated endogenous proteins. SGTA served as loading control as well as an internal control for equal Bag6 co-immunoprecipitation potential. In Bi, the EMC2 and EMC1 bands are indicated by arrows. Arrow in Bii and C indicates full-length MAVS. Open circles on MAVS blots indicate signals derived from denatured antibody heavy and light chains. (D) Mean±s.e.m. of MAVS levels that co-immunoprecipitate with Bag6 in siEMC5-treated cells relative to nt siRNA-treated cells for four independent experiments as shown in C. *$P<0.05$ (paired two-tailed t-test).

induced activation of MAVS-mediated signalling (Ren et al., 2020), prolonged poly(I:C) stimulation resulted in a substantial ∼70% reduction in membrane-associated MAVS after 24 h (Fig. 6Bi,ii). In contrast, the relative amount of MAVS recovered in the cytosol was unaltered across the same 24 h time-course (Fig. 6Bi,iii). Interestingly, the proportion of this cytosolic pool of MAVS that

was recovered with Bag6 initially showed a transient decline of ∼30% at 4 h and 12 h after stimulation, but returned to its initial level at 24 h (Fig. 6C,D). These data show that the population of MAVS that is bound to the BAG6 complex is dynamic and may respond to the activation of innate immune signalling following viral infection.
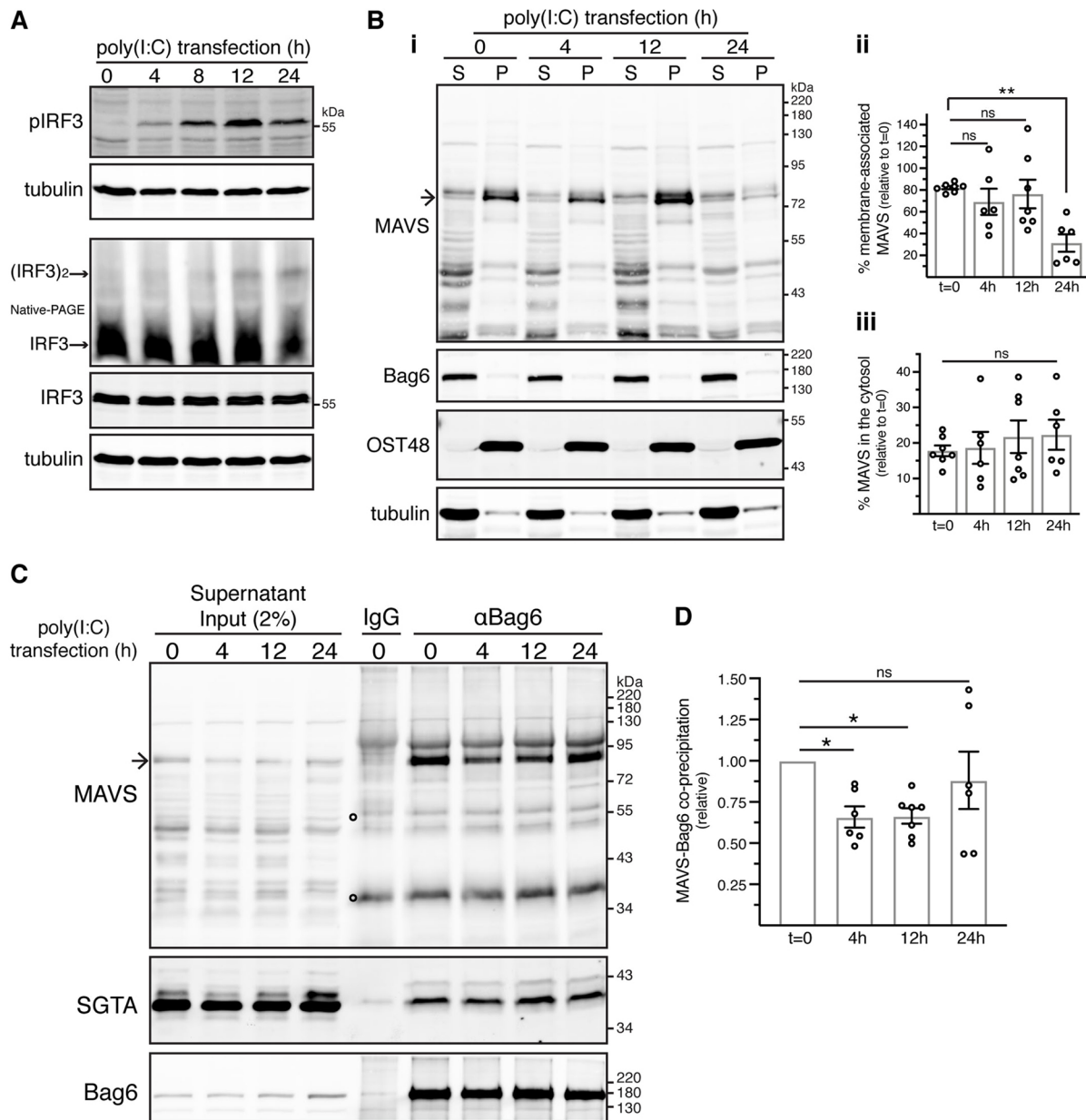
Fig. 6. Stimulation with poly(I:C) compromises the Bag6–MAVS interaction. (A) Kinetics of IRF3 activation in response to cytosolic poly(I:C). Control KO cells were mock-transfected (*t*=0) or transfected with poly(I:C) for various times before immunoblotting for the indicated proteins. Activation of endogenous IRF3 was assessed by induction of its phosphorylation and dimerisation. Phosphorylated IRF3 blot is representative of six independent experiments. Western blot for the detection of IRF3 dimer is representative of two independent experiments. pIRF3, phosphorylated IRF3; (IRF3)2, IRF3 dimer. (B) Stimulation with cytosolic poly(I:C) does not grossly alter the levels of MAVS in the crude cytosolic supernatant fraction. (i) Control KO cells were mock-transfected (*t*=0) or transfected with poly(I:C) for various times before their fractionation as shown in Fig. 2A. The resulting supernatant (S) and pellet (P) fractions were analysed by immunoblotting for the indicated endogenous proteins. (ii,iii) Mean±s.e.m. of the (ii) pellet/total ratio and (iii) supernatant/total ratio of MAVS levels in poly(I:C)-transfected cells relative to the respective ratios in mock-transfected cells (*t*=0) for six independent experiments as in Bi. **$P<0.01$; ns, not significant (ordinary one-way ANOVA with Dunnett's multiple comparison tests). (C) Cytosolic poly(I:C) impairs Bag6–MAVS interaction. Supernatant fractions from Bi were subjected to immunoprecipitations with rabbit anti-Bag6 antibody (αBag6) or rabbit control IgG antibody. Inputs and immunoprecipitates were analysed by immunoblotting for the indicated endogenous proteins. SGTA served as loading control as well as internal control for comparable Bag6 binding. Arrow in MAVS blot in Bi and C indicates full-length MAVS. Open circles on MAVS blots indicate signals derived from denatured antibody heavy and light chains. (D) Mean±s.e.m. of MAVS levels that co-immunoprecipitate with Bag6 in poly(I:C)-transfected relative to mock-transfected cells (*t*=0) for six independent experiments as shown in C. *$P<0.05$; ns, not significant (one-way ANOVA with Dunnett's multiple comparison tests).

DISCUSSION

SGTA and the BAG6 complex are early TMD-recognition factors acting on the major pathway for TA targeting to the ER (Casson et al., 2017; Farkas and Bohnsack, 2021; Hegde and Keenan, 2021). In this study, we have identified the mitochondrial TA protein MAVS as an endogenous client of both SGTA and the BAG6 complex. The TMD region of MAVS is essential for its binding to SGTA, consistent with its dynamic engagement of newly synthesised TA proteins (Casson et al., 2017; Farkas and Bohnsack, 2021; Hegde and Keenan, 2021), including Stx-5, which is destined

for the ER. Although MAVS is primarily localised to the MOM, it is also found at both MAMs [i.e. ER domains juxtaposed to discrete sites on mitochondria (Wu et al., 2018)] and peroxisomes (Horner et al., 2011). Although the combination of a moderately hydrophobic TMD and a positively charged C-terminal region (Fig. S4C) are necessary to reach these distinct locations (Dixit et al., 2010), it is unclear exactly how such diversity of targeting is achieved for MAVS.

Previous studies suggest that some newly synthesised TA proteins that are destined for mitochondria, such as OMP25, are bound by cytosolic ubiquilins, which can prevent their aggregation prior to insertion into the MOM (Itakura et al., 2016). However, we were unable to find any evidence of a stable interaction between the ubiquilins and OMP25 or MAVS in our experimental system (Fig. S5), leaving open their contribution to the biogenesis of TA proteins destined for the MOM (Fig. 7, pathway 1). In contrast to OMP25, we recover a pool of cytosolic MAVS bound to the BAG6 complex, most likely acting downstream of SGTA, which can capture nascent TA clients as their hydrophobic TMDs emerge from the ribosomal exit tunnel (Leznicki and High, 2020) (Fig. 7, pathway 2). In further support of this model, we recover less Bag6-bound MAVS in SGTA KO cells as compared to control cells (Fig. 3B,C). Nevertheless, SGTA is clearly dispensable for MAVS binding to the BAG6 complex, suggesting that there are alternative mechanisms for loading MAVS onto the BAG6 complex (Fig. 7, pathway 3).

The selective binding of MAVS to the BAG6 complex in cytosolic extracts (Fig. S4, cf. OMP25) most likely reflects a stable interaction between MAVS and the Bag6 subunit of the heterotrimeric BAG6 complex, which acts as a holdase that can also initiate the selective ubiquitylation of aberrant clients such as MLPs (Leznicki et al., 2013; Rodrigo-Brenni et al., 2014; Wang
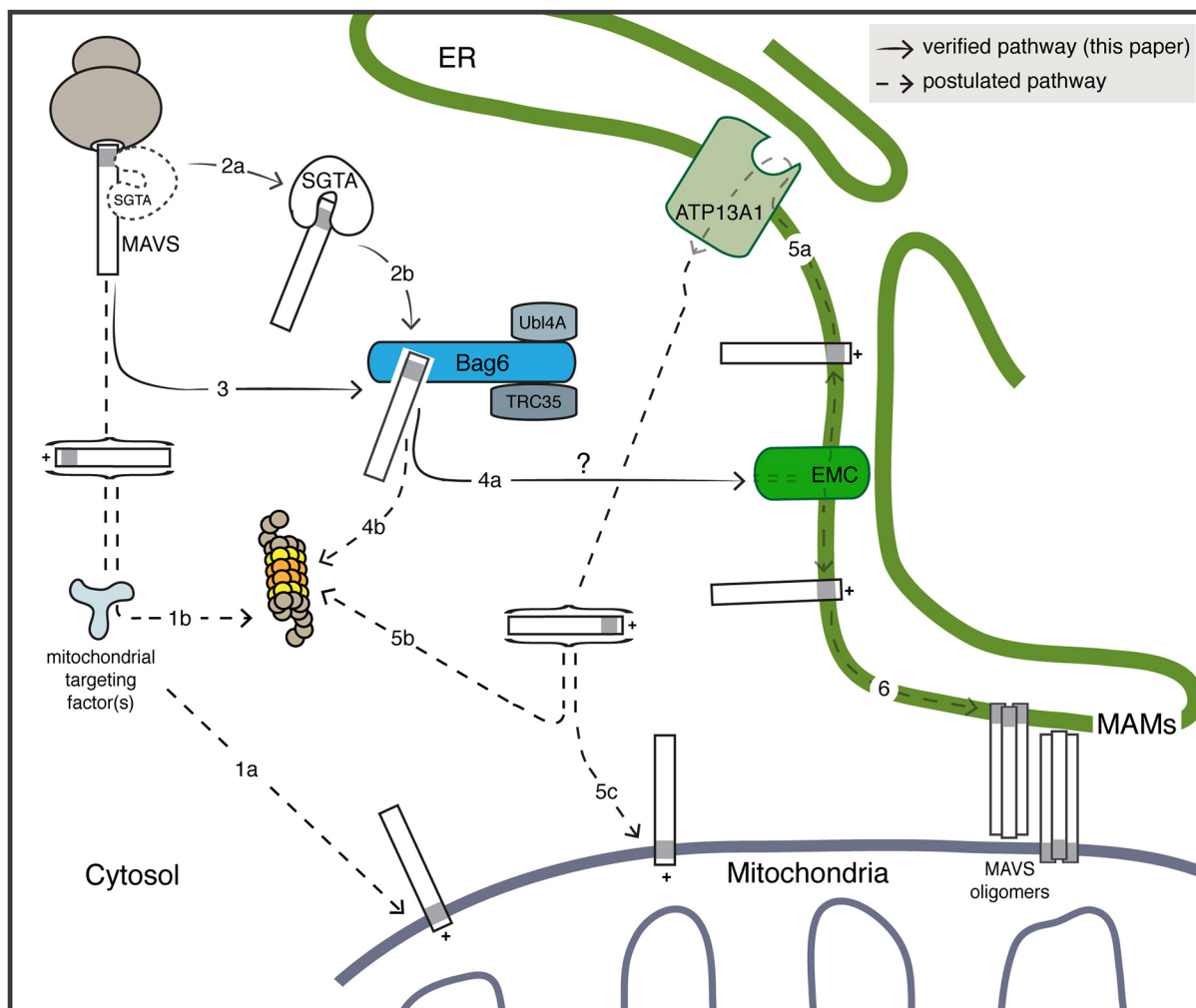
Fig. 7. Working model for the role of the BAG6 complex during MAVS biogenesis. The molecular basis for the post-translational targeting and insertion of TA proteins such as MAVS into the mitochondrial outer membrane (MOM) are poorly defined (Bykov et al., 2020) (pathway 1a). Failed mitochondrial import can result in the mislocalisation of MAVS to the cytosol, where it may be recognised by one or more quality control machineries and targeted for proteasomal degradation (Itakura et al., 2016) (pathway 1b). A fraction of newly synthesised MAVS also engages the BAG6 complex either directly (pathway 3) or after transfer from SGTA (pathway 2). In the later case, SGTA may bind MAVS as its TMD leaves the ribosomal exit tunnel or after its release into the cytosol (Leznicki and High, 2020). The BAG6 complex acts upstream of MAVS 'misinsertion' into the ER membrane, which is most likely facilitated by the EMC (pathway 4a). It is currently unknown whether additional factors act between the BAG6 complex and the EMC insertase (pathway 4a, see ?). BAG6 binding might also enable the proteasomal degradation of mislocalised MAVS (Rodrigo-Brenni et al., 2014) (pathway 4b). At the ER membrane, 'mistargeted' MAVS can be recognised by the P5A-ATPase ATP13A1 and extracted to the cytosol (McKenna et al., 2020) (pathway 5a) for either proteasomal degradation (pathway 5b) or reinsertion into the MOM via an ER-SURF pathway (Hansen et al., 2018) (pathway 5c). The access of an ER-localised pool of MAVS to ER-MOM contacts sites (MAMs) that facilitate MAVS oligomerisation and downstream signalling (Esser-Nobis et al., 2020) (pathway 6) may be modulated by the innate immune response.

et al., 2011). This stable binding of MAVS to the Bag6 subunit is distinct from the fate of SGTA-bound clients that are on a productive pathway for ER targeting (Casson et al., 2016). In this case, the Ubl4A subunit of the BAG6 complex facilitates a rapid and privileged transfer of these TA proteins from SGTA directly to TRC40 (Mock et al., 2015; Shao et al., 2017). However, although MAVS is detected in both the MOM and the ER (Esser-Nobis et al., 2020), it was neither bound by a TRC40 trap mutant nor affected by co-depletion of TRC40 and WRB (Coy-Vergara et al., 2019). Hence, in contrast to Stx-5 and other TA proteins that are efficiently targeted to the ER, the biogenesis of MAVS is TRC40 independent (Coy-Vergara et al., 2019).

Taken with our own findings, these data suggest that SGTA binds to MAVS but is unable to hand it off to TRC40, and therefore relies on alternative downstream acceptors for this client, including the Bag6 subunit of the BAG6 complex. This model is in good agreement with the suggestion that the BAG6 complex acts as a sortase that directs hydrophobic MLPs towards either ER targeting or selective degradation, depending on the ability of TRC40 to receive SGTA-bound clients (Casson et al., 2016; Farkas and Bohnsack, 2021). Knockdown of the Bag6 protein has no clear effect on steady-state levels of MAVS, nor does it result in the formation of detergent-insoluble aggregates (Fig. S7). However, any contribution of the BAG6 complex to its proteasomal degradation (Fig. 7, pathway 4b) may well be redundant (Rodrigo-Brenni et al., 2014). We therefore conclude that the BAG6 complex more likely acts as a 'holdase' for mislocalised cytosolic MAVS that shields its hydrophobic TA region (Itakura et al., 2016; Wang et al., 2011). Whether BAG6-bound MAVS is maintained in a soluble conformation that is competent for subsequent membrane insertion and/or whether this specific pool of MAVS can be selectively ubiquitylated to enable its proteasomal degradation (Fig. 7, pathway 4) will require further detailed studies (see Casson et al., 2016; Farkas and Bohnsack, 2021; Hegde and Keenan, 2021).

In order to address at what stage of MAVS biogenesis it can interact with the BAG6 complex, we perturbed a defined pool of MAVS that mislocalises to the ER membrane (McKenna et al., 2020). When the P5-ATPase-dependent extraction of ER-localised MAVS was perturbed by knocking down ATP13A1 (McKenna et al., 2020), we found no reduction in the amount of MAVS that was recovered with the BAG6 complex (Fig. 4). However, when the EMC-dependent misinsertion of MAVS into the ER membrane was inhibited by knocking down the EMC5 subunit, a significant increase in the cytosolic pool of BAG6-bound MAVS was observed (Fig. 5). On this basis, we conclude that MAVS is engaged by BAG6 prior to its misinsertion into the ER membrane via an EMC-dependent pathway (Fig. 7, pathway 4) that likely reflects the structural conservation of the EMC and the WRB–CAML complex (McDowell et al., 2020).

Although the delivery of mitochondrial TA proteins to the ER membrane is typically described as mislocalisation, it has now been established that a subset of membrane proteins can be productively redirected to the MOM from the ER via a process known as ER-SURF (Koch et al., 2021). It is currently unclear whether mitochondrial TA proteins, including MAVS and OMP25, are competent for onward delivery to the MOM following their ATP13A1-dependent extraction from the ER (Fig. 7, pathway 5) (see Farkas and Bohnsack, 2021; McKenna et al., 2020). Hence, it is possible that SGTA, the BAG6 complex and the EMC enable the ER insertion of MAVS proteins that are on a productive route to the MOM via the ER (Fig. 7, pathways 2–5). It should also be noted that a pool of MAVS, which localises to ER–MOM contact sites

(MAMs), has been proposed to play a key role in initiating the innate immune response to viral infection (Esser-Nobis et al., 2020; Thoresen et al., 2021). The mechanism(s) by which such a MAM-localised pool of MAVS is generated remains undefined and we propose that one function of a BAG6- and EMC-mediated pathway for ER insertion may be to provide a subpopulation of ER-localised MAVS that is competent for sorting into such ER-MOM contacts (Fig. 7, pathway 6). Hence, following insertion into the ER, the MAVS protein may have access to multiple fates that are regulated by prevailing cellular conditions including viral infection. In this context, when an artificial innate immune response that activates MAVS-dependent signalling is induced (Fig. 6A), we initially observe a significant reduction in the cytosolic pool of MAVS that is recovered with the BAG6 complex (Fig. 6). However, this pool of BAG6-bound MAVS returns to its pre-stimulation level after 24 h, reflecting a reduction in downstream IRF3 phosphorylation (Fig. S6A) that is observed over the same time frame (Fig. 6). Thus, the pool of BAG6-bound MAVS that we identify in this study appears to be subject to temporal regulation during the innate immune signalling process, perhaps allowing for the fine-tuning of MAVS availability in selected organellar membranes (see Vazquez and Horner, 2015) (Fig. 7). Further studies will be required to establish whether this BAG6-bound pool of MAVS plays any specific role in the propagation of RIG-I-like receptor-dependent signalling following viral infection (Thoresen et al., 2021).

MATERIALS AND METHODS
Antibodies and reagents
Anti-Bag6 rabbit polyclonal antibodies [1:1000 for immunoblotting (IB); 1:100 for immunoprecipitation (IP)] were raised against a synthetic peptide corresponding to residues 112–130 of human Bag6 isoform 2 (GSPPGTRGPGASVHDRNAN; synthesised by Peptide Specialty Laboratories GmbH) and affinity purified (also described in Leznicki et al., 2013). Anti-SGTA chicken polyclonal antibodies (1:2500 for IB; 1:200 for IP) were raised against recombinant His-thioredoxin-SGTA and affinity purified (also described in Leznicki et al., 2015). Other antibodies used were as follows: anti-ATP13A1 (Proteintech 16244-1-AP, Lot 00007441; 1:2500 for IB), anti-Bag6 (Abnova H00007917-B01P, Lot J9271; 1:5000 for IB), anti-calnexin (Cell Signaling Technology #2679, Lot 4; 1:1000 for IB), anti-EMC1 (Abgent AP10226b, Lot SA100702BL; 1:500 for IB), anti-EMC2 (Santa Cruz Biotechnology sc-166011; 1:500 for IB), anti-EMC5 (Bethyl Laboratories A305-832A-M; 1:1000 for IB), anti-HA [Covance MMS-101R, Lot 14811501; 1:1000 for IB; 1:500 for immunofluorescence (IF)], anti-His (Sigma H1029, Lot 106M4768V; 1:3000 for IB), anti-Hsp70 (Abcam ab47455, Lot GR166016-49; 1:5000 for IB), anti-Hsp90 (Enzo Life Sciences ADI-SPA-846, Lot 07061528; 1:2000 for IB), anti-IRF3 (Cell Signaling Technology #11904, Lot 6; 1:1000 for IB), anti-phospho-IRF3 (Cell Signaling Technology #4947, Lot 13; 1:1000 for IB), anti-MAVS (Santa Cruz Biotechnology sc-166583, Lot L3119 and Lot C0421; 1:1000 for IB), anti-MAVS (Enzo Life Sciences ALX-210-929-C100, Lot 08061948; 1:100 for IP), anti-Myc (Merck Millipore 05-724, Lot 3095953; 1:5000 for IB), anti-Myc (Cell Signaling Technology #2276, Lot 24; 1:2000 for IF), anti-OMP25 (Proteintech 15666-1-AP, Lot 00068490; 1:1000 for IB), anti-OST48 [previously described (Roboti and High, 2012); 1:1000 for IB], anti-SGTA (Santa Cruz Biotechnology sc-130557, Lot E0809; 1:500 for IB), anti-Stx-5 (Synaptic Systems 110053, Lot 1-18 and Lot 110053/15; 1:5000 for IB, 1:100 for IP), anti-Stx-5 (Santa Cruz Biotechnology sc-365124, Lot H1419; 1:500 for IB), anti-TOM20 (Santa Cruz Biotechnology sc-17764, Lot H0320; 1:500 for IB), anti-TRC35 (Bethyl Laboratories A302-613A, Lot 1; 1:1000 for IB), anti-tubulin (gift from Keith Gull, University of Oxford, UK; 1:1000 for IB), anti-ubiquilin (Invitrogen 37-7700, Lot RJ241978; 1:1000 for IB), anti-ubiquilin-2 (Abcam ab217056, Lot GR3185004-6; 1:2000 for IB, 1:100 for IP), anti-rabbit IgG (Santa Cruz Biotechnology sc-2027, Lot F2413; 1:40 for IP) and anti-chicken IgY (Santa Cruz Biotechnology sc-2718, Lot

L1412; 1:40 for IP). For infrared IB, IRDye 680LT/800CW-conjugated secondary antibodies (1:5000) raised in donkey were purchased from LI-COR BioSciences. For IF, Alexa Fluor 488-conjugated streptavidin (1:200) and Alexa Fluor 594-conjugated donkey anti-rabbit IgG antibodies (1:800) were purchased from Jackson ImmunoResearch Laboratories. Other commercially available reagents were: PMSF (Sigma-Aldrich 93482; 1 mM final), protease inhibitor cocktail (Sigma-Aldrich P8340; 1:100), phosphatase inhibitor cocktail set II (Calbiochem 524625; 1:100), benzonase nuclease (Millipore 70746; 250 U final) and EasyTag EXPRESS [^{35}S]Met/Cys mix (PerkinElmer NEG772014MC).

Plasmids and siRNA oligonucleotides
SGTA-V5 and PEX19-V5 in pcDNA5/FRT/V5-His-TOPO were previously described (Leznicki and High, 2012; Leznicki et al., 2015; Payapilly and High, 2014). pcDNA3.1-Myc-BioID2 (#74223) and pcDNA3.1-BioID2-HA (#74224) plasmids were obtained from Addgene. The sequences encoding SGTA-V5 and PEX19-V5 were amplified from pcDNA5 and inserted into the NheI-AgeI sites of pcDNA3.1-BioID2-HA. The plasmids encoding substrate$_{bd}$mt and (UBL$_{bd}$ & TPR$_{d}$)mt SGTA-V5-BioID2-HA were generated by site-directed mutagenesis with PfuTurbo DNA polymerase (Agilent Technologies). Full-length human MAVS cDNA was transferred from pGEM-MAVS (Sino Biological HG15224-G) into the KpnI-NotI sites of the pCMV6-Entry vector (OriGene Technologies #PS100001) and an N-terminal FLAG tag was introduced by site-directed mutagenesis. The CARD (residues 10–77) and TMD (residues 514–535) were deleted from the FLAG–MAVS coding sequence by inverse PCR. The siRNA oligonucleotides used were: ON-TARGETplus non-targeting control pool (Dharmacon D-001810-10-20), ON-TARGETplus human siATP13A1 (Dharmacon J-020426-06-0020), siEMC5 (ThermoFisher Scientific s41129), siBag6#1 [5′-CAGCUCCGGUCUGAUAUACAA-3′ (Winnefeld et al., 2006)], siBag6#2 [5′-UUUCUCCAAGAGCAGUUUA-3′ (Minami et al., 2010)] and siBag6#3 (5′-GCUCUAUGGCCCUUCCUCA-3′). The siBag6 duplexes were made to order as 'ON-TARGETplus' by Dharmacon.

Cell culture and transfection
Parental HepG2 cells (ATCC #85011430) and HepG2-derived KO cell lines were cultured in high-glucose Dulbecco's modified Eagle's medium (DMEM; Sigma-Aldrich) supplemented with 10% (v/v) fetal bovine serum (FBS; Sigma-Aldrich) at 37°C, 5% CO_2 in a humidified incubator. Cells were routinely tested for mycoplasma contamination. DNA transfection was performed using Lipofectamine 3000 (Thermo Fisher Scientific) by preparing a DNA solution containing P3000 reagent (1.5 µl/µg DNA), and then forming complexes of DNA:Lipofectamine 3000 at a ratio of 2:3. Transfection with poly(I:C) (Invivogen #tlrl-pic; 1 µg/ml final) was performed using Lipofectamine 3000 as described above. For siRNA transfection, cells were transfected with 25 nM siRNA oligonucleotides using Lipofectamine RNAiMAX (ThermoFisher Scientific) according to the manufacturer's instructions.

Generation of SGTA KO cells
KO cell lines were generated using the CRISPR-Cas9 system as described previously (Ran et al., 2013). Briefly, two double-stranded oligonucleotides targeting exon 2 of human SGTA (guide #1: 5′-CATGACCAGCTCCGG-CACGG-3′ and guide #2: 5′-CAGGAACTGGATGATGGCGT-3′) were ligated into the pSpCas9(BB)-2A-puro vector (Addgene #62988) using BbsI sites. HepG2 cells plated at 5×10^5 cells per 3.5 cm dish were grown for 20 h before transfection with 2.5 µg of the resultant single-guide RNA (sgRNA) expression constructs using Lipofectamine 3000. At 24 h post transfection, transfected cells were selected by a 72 h incubation in medium supplemented with puromycin 1 µg/ml. Puromycin-resistant cells were seeded into 96-well plates at 0.8 cells per well, and clonal cell lines screened for SGTA deficiency by IB and genomic sequencing.

Immunoblotting
Denatured proteins were separated by SDS-PAGE and transferred to Immobilon-FL PVDF membranes (Merck Millipore IPFL00010). Membranes were incubated in a casein-based blocking buffer (Sigma-

Aldrich) for 1 h and subsequently with primary antibodies in blocking buffer [Tris-buffered saline supplemented with 0.1% (v/v) Tween-20; TBST] for >12 h at 4°C. After three washes with TBST, membranes were incubated with secondary antibodies in TBST supplemented with 0.01% (v/v) SDS for 1 h at room temperature. For detecting biotinylated proteins, blocked membranes were incubated with IRDye800CW-conjugated streptavidin (LI-COR BioSciences 926-32230; 1:5000) for 1 h at room temperature. Membranes were washed extensively with TBST and fluorescent bands visualised on an Odyssey CLx Infrared Imager (LI-COR Biosciences). Signals were quantified using the automatic background subtraction function (setting: average, top and bottom) of the Image Studio Lite 5.2.5 software provided by the manufacturer. The relative amount of MAVS in the supernatant fraction that co-immunoprecipitated with Bag6 was calculated as follows. Firstly, the quantified signals for MAVS and Bag6 species in Bag6 IPs were corrected to account for any background by subtracting the respective signals in the IgG controls. The ratio of the corrected MAVS signal to the corrected Bag6 signal was then calculated to provide a proxy for the relative amount of MAVS that was bound to Bag6 under different treatment conditions. These values were then expressed relative to the respective value obtained using control cells, which was arbitrarily set to one (see Figs 3C, 4D–6D). Quantification of cytosolic and membrane-associated MAVS was performed as follows. MAVS signals in the supernatant and pellet fractions were normalised to tubulin and OST48 loading controls, respectively. The ratio of the normalised MAVS signal in each fraction to the total MAVS signal was then calculated, and the resulting value was expressed relative to the respective value in control cells (see Figs 4B–6B).

BioID2 labelling and streptavidin-affinity purification
A 2.05 mM biotin (Sigma-Aldrich B4501) stock was prepared in distilled water by brief sonication. Cells were seeded into 15 cm dishes at 7.5×10^6 cells per dish and grown for ~20 h before transfection with 30 µg of the indicated BioID2-tagged expression construct. At ~36 h post transfection, cells were incubated with fresh medium supplemented with 50 µM biotin and harvested 8 h later. Cell pellets from two 15 cm dishes were solubilised in 1 ml RIPA buffer [50 mM Tris-HCl pH 7.5, 150 mM NaCl, 1 mM EDTA, 1 mM EGTA, 1% (v/v) IGEPAL CA-630, 0.5% (w/v) sodium deoxycholate and 0.1% (v/v) SDS] supplemented with PMSF, protease inhibitors and benzonase by continuous shaking at 4°C for 1 h. The lysates were sonicated (3×10 s bursts with 5 s rest) on ice at low amplitude in a Bioruptor (Diagenode) and then centrifuged at 20,817 **g** for 30 min at 4°C. The post-nuclear supernatants were further diluted in RIPA buffer to 2.5 mg total protein per ml, and biotinylated proteins were affinity-purified by incubation with streptavidin-Sepharose beads (Cytiva 17-5113-01; 8 µl 1:1 slurry per mg of total protein) at 4°C on a nutator for 3 h. The beads were pelleted (400 **g**, 5 min) and washed four times with RIPA buffer and three times with 50 mM ammonium bicarbonate, pH 8.0. After all residual ammonium bicarbonate was pipetted off, beads were flash-frozen and stored at −80°C before shipping to the Proteomics Core facility at Sanford-Burnham-Prebys Medical Discovery Institute.

On-beads protein digestion and LC-MS/MS analysis
Liquid-free beads were resuspended in 8 M urea dissolved in 50 mM ammonium bicarbonate, and disulphide bonds were reduced with 10 mM tris(2-carboxyethyl)phosphine at 30°C for 60 min. After cooling the samples to room temperature, free cysteines were alkylated with 30 mM iodoacetamide for 30 min in the dark. Following alkylation, urea was diluted to 1 M using 50 mM ammonium bicarbonate, and proteins were subjected to overnight digestion with Mass Spec Grade Trypsin/Lys-C mix (Promega). The beads were then pulled down and the solutions containing the digested peptides were desalted using AssayMap C18 cartridges mounted on an AssayMap Bravo liquid handling system (Agilent Technologies) and subsequently dried down in a SpeedVac concentrator.

Prior to liquid chromatography tandem mass spectrometry (LC-MS/MS) analysis, dried peptides were reconstituted in 2% (v/v) acetonitrile, 0.1% (v/v) formic acid, and their concentration was determined using a NanoDrop spectrophotometer (Thermo Fisher Scientific). Samples were then analysed

by LC-MS/MS using a Proxeon EASY-nanoLC system (Thermo Fisher Scientific) coupled to a Q Exactive Plus Orbitrap mass spectrometer (Thermo Fisher Scientific). Peptides were resolved on a 250 mm×75 µm Aurora C18 reversed-phase analytical column (IonOpticks) over a 120 min organic gradient (1–5% solvent B over 1 min, 5–23% solvent B over 72 min, 23–34% solvent B over 45 min and 34–48% solvent B over 2 min) with a flow rate of 300 nl/min (60°C). Solvent A was 0.1% formic acid and solvent B was 80% acetonitrile in 0.1% formic acid. The mass spectrometer was operated in positive data-dependent acquisition mode. MS1 spectra were measured in the Orbitrap with a resolution of 70,000 (at m/z 400) in the mass range m/z 350–1700. Automatic gain control (AGC) target was set to 1×10^6 with a maximum injection time of 100 ms. Up to 12 MS2 spectra per duty cycle were triggered, fragmented by HCD, and acquired at a resolution of 17,500 and an AGC target of 5×10^4, an isolation window of 1.6 m/z and a normalised collision energy of 25. The dynamic exclusion was set to 20 s with a 10 ppm mass tolerance around the precursor.

MS data analysis

Raw data were analysed using MaxQuant software (v1.5.5.1) searching against the Uniprot *Homo sapiens* database (downloaded in January 2019) and the GPM cRAP database containing common contaminants (https://www.thegpm.org/crap/). Precursor mass tolerance was set to 20 ppm for the first search, where initial mass recalibration was completed, and to 4.5 ppm for the main search. Product ions were searched with a mass tolerance of 0.5 Da. The maximum precursor ion charge state used for searching was 7. Cysteine carbamidomethylation was set as a fixed modification, while oxidation of methionine and acetylation of protein N-terminus were set as variable modifications. Enzyme was set to trypsin in a specific mode and a maximum of two missed cleavages was allowed for searching. The target-decoy-based false discovery rate (FDR) filter for spectrum and protein identification was set to 0.01. Protein label-free quantification (LFQ) intensities were exported from MaxQuant and analysed through SAINTexpress software (v3.6.3) (Teo et al., 2014) using default parameters to identify proximal interactions. Controls were set as both Myc–BioID2 and PEX19–BioID2 samples. High-confidence bait–prey interactions were identified using a BFDR (Bayesian FDR) threshold of 0.05. Mass spectrometry data are available via ProteomeXchange with identifier PXD030129.

Immunofluorescence analysis

Cells plated on coverslips at 5×10^5 cells per 3.5 cm dish were transfected with 2.5 µg of the indicated plasmid using Lipofectamine 3000. At 36 h post transfection, cells were fixed with 4% (v/v) paraformaldehyde in phosphate-buffered saline (PBS) for 30 min at room temperature and unreacted aldehyde groups quenched with 0.1 M glycine-Tris pH 8.5 for 12 min. Cells were then permeabilised with 0.1% (v/v) Triton X-100 for 5 min at room temperature and washed twice prior to incubation with primary antibodies in PBS for 1 h. Three washes with PBS followed before a further 1 h incubation with secondary antibody solution supplemented with the DNA dye DAPI. After cells were washed with PBS, coverslips were dried and mounted on slides with ProLong Gold Antifade reagent (Thermo Fisher Scientific). Imaging was performed using an Olympus BX60 upright microscope using a 100× oil-immersion objective and equipped with a MicroMax cooled, slow-scan CCD camera (Roper Scientific) driven by Metaview software (University Imaging Corporation). Images were processed with ImageJ.

Cell fractionation and co-immunoprecipitation analysis

Three million cells were plated per 15 cm dish and harvested after ∼96 h. For cytosolic delivery of poly(I:C), cells were transfected 72 h after plating and harvested 4–24 h later. For knockdown experiments, cells plated at 7.5×10^6 cells per 15 cm dish were transfected 20 h after plating and harvested 72 h post transfection. Cell pellets were resuspended in 5× volumes of buffer A (50 mM Tris-HCl pH 7.5, 150 mM NaCl and 1.5 mM MgCl$_2$) supplemented with PMSF, protease and phosphatase inhibitors. The cell suspension was kept on ice for 30 min and then homogenised by 22 passes through a cell homogenizer (Isobiotec, Germany) with a tungsten

carbide ball (clearance of 10 µm). The crude homogenate was subjected to two rounds of centrifugation at 700 g for 10 min at 4°C and the resulting post-nuclear supernatant was further centrifuged at 21,380 g for 30 min at 4°C to obtain a supernatant (crude cytosol) and a pellet (crude membranes) fraction. The supernatant fraction and the buffer A-washed pellet fraction were centrifuged again at 21,380 g for 30 min at 4°C to remove contaminants. The supernatant fraction was then incubated with 5 µg of the indicated antibodies and protein A-agarose beads (GenScript L00210) at 4°C on a nutator for 5 h. After washing the beads four times with buffer A, bound proteins were eluted with 2× SDS sample buffer and analysed by infrared IB.

Pulse–chase analysis of protein secretion

The secretion assay was performed using a pulse–chase approach as previously described (Roboti et al., 2013). Briefly, cells were left untreated or treated with 2.5 µg/ml brefeldin A (Sigma-Aldrich B7651) for 1 h before being starved in Met- and Cys-free DMEM (starvation medium; Thermo Fisher Scientific 21013024) for 20 min at 37°C. Labelling was initiated by addition of fresh starvation medium containing 22 mCi/ml [^{35}S]Met/Cys for 15 min. After washing with PBS, cells were incubated in serum-free DMEM supplemented with 2 mM unlabelled L-Met and L-Cys for 2 h. Brefeldin A was included throughout the starvation, pulse and chase. Secreted proteins in the medium were recovered by precipitation with 13% trichloroacetic acid, washed in acetone and dissolved in 2× SDS sample buffer. Cells were solubilised with Triton X-100 lysis buffer [20 mM Tris-HCl pH 7.5, 150 mM NaCl, 1% (v/v) Triton X-100, 1 mM EDTA and 1 mM EGTA] supplemented with PMSF and protease inhibitors. Equal amounts of precipitated proteins in the media and clarified lysates were analysed by SDS–PAGE and phosphorimaging using FLA-3000 (Fujifilm).

In vitro transcription, translation and pull-down assay

Linear DNA templates were generated by PCR using appropriate primers and transcribed into mRNA with T7 polymerase (Promega). *In vitro* translation was performed in rabbit reticulocyte lysate (Promega) supplemented with 1 mCi/ml [^{35}S]Met/Cys, amino acid mix lacking Met (Promega) and 0.1× volume of an *in vitro* transcribed mRNA (200-1000 ng/µl) in the absence or presence of 2 µM recombinant His-S-tag-SGTA (gift from Pawel Leznicki, Sygnature Discovery, UK) for 90 min at 30°C. Following a 10 min incubation with 1 mM puromycin (Sigma-Aldrich P7255) at 37°C, the reactions were diluted 5.5-fold with buffer B [50 mM HEPES-KOH pH 7.5, 300 mM NaCl, 10 mM imidazole and 10% (v/v) glycerol] and incubated with pre-equilibrated HisPur Cobalt resin (Thermo Fisher Scientific) at 4°C for 2 h. After washing the beads, bound proteins were eluted with buffer B supplemented with 200 mM imidazole. Samples were resolved by SDS-PAGE and radiolabelled products visualised by phosphorimaging using FLA-3000 (Fujifilm).

Analysis of dimeric and phosphorylated state of IRF3

Native PAGE gels (7.5%) were pre-run with running buffer [25 mM Tris-HCl pH 8.4 and 192 mM glycine in the presence of or absence of 0.5% (w/v) sodium deoxycholate in the cathode and anode buffer, respectively] at 120 V in a cold room for ∼35 min. Cells from confluent 3.5 cm dishes were lysed with ice-cold buffer A supplemented with 0.5% (v/v) IGEPAL CA-630, PMSF, protease and phosphatase inhibitors. The cell extracts were kept on ice for 30 min before centrifugation at 21,380 g for 10 min to remove the insoluble fraction. The clarified cell lysates were then mixed with 5× native sample buffer [250 mM Tris-HCl pH 6.8, 1% (w/v) sodium deoxycholate, 50% (v/v) glycerol and 0.5% (w/v) Bromophenol Blue] to a final concentration of 1×, and immediately loaded on the gel and run at 120 V for 100 min in a cold room. The monomeric and dimerised IRF3 were detected by infrared IB.

For detection of phosphorylated IRF3, cells from confluent 3.5 cm dishes were solubilised in ice-cold RIPA buffer supplemented with PMSF, benzonase, protease and phosphatase inhibitors by continuous shaking at 4°C for 1 h. The lysates were sonicated (3×10 s bursts with 5 s rest) on ice at low amplitude in a Bioruptor (Diagenode) and then centrifuged at 20,817 g for 30 min at 4°C. Clarified lysates (∼150 µg total protein) were resolved by

SDS-PAGE and analysed by infrared IB. Note that incubation of blots with anti-phospho-IRF3 was performed in 5% bovine serum albumin in TBST overnight at 4°C.

Detergent solubility assay

The solubility assay was performed as described previously (Itakura et al., 2016) with minor modifications. Cells were lysed with ice-cold, non-denaturing lysis buffer [50 mM Tris-HCl pH. 7.4, 150 mM NaCl, 1 mM EDTA, 0.5% (v/v) IGEPAL CA-630 and 0.5% (w/v) sodium deoxycholate] supplemented with PMSF and protease inhibitors by gentle shaking at 4°C for 30 min. After centrifugation at 20,817 g for 30 min at 4°C, the post-nuclear supernatants (soluble fractions) were collected in a separate tube and the pellets (insoluble fractions) were dissolved in an equal volume of ice-cold RIPA buffer supplemented with PMSF, protease inhibitors and benzonase by vigorous shaking at 4°C for 1 h. Following a brief sonication step of the insoluble fractions on ice, both the soluble and the insoluble fractions were denatured in SDS sample buffer and analysed by infrared IB.

Statistics

All experiments were repeated at least three times with representative data shown. Data are expressed as the mean±s.e.m. and significant differences among two or multiple experimental groups were assessed by the indicated two-tailed t-test and one-way ANOVA, respectively. Statistical analyses and data plotting were performed using GraphPad Prism 9.

Author contributions

Conceptualization: S.H.; Software: C.L.; Validation: P.R.; Formal analysis: P.R., C.L.; Investigation: P.R.; Writing - original draft: P.R., S.H.; Writing - review & editing: P.R., C.L., S.H.; Visualization: P.R.; Supervision: S.H.; Project administration: S.H.; Funding acquisition: S.H.

References

Antonicka, H., Lin, Z.-Y., Janer, A., Aaltonen, M. J., Weraarpachai, W., Gingras, A.-C. and Shoubridge, E. A. (2020). A high-density human mitochondrial proximity interaction network. *Cell Metab.* **32**, 479-497.e9. doi:10.1016/j.cmet.2020.07.017

Benarroch, R., Austin, J. M., Ahmed, F. and Isaacson, R. L. (2019). The roles of cytosolic quality control proteins, SGTA and the BAG6 complex, in disease. *Adv. Protein Chem. Struct. Biol.* **114**, 265-313. doi:10.1016/bs.apcsb.2018.11.002

Brambillasca, S., Yabal, M., Soffientini, P., Stefanovic, S., Makarow, M., Hegde, R. S. and Borgese, N. (2005). Transmembrane topogenesis of a tail-anchored protein is modulated by membrane lipid composition. *EMBO J.* **24**, 2533-2542. doi:10.1038/sj.emboj.7600730

Bykov, Y. S., Rapaport, D., Herrmann, J. M. and Schuldiner, M. (2020). Cytosolic Events in the Biogenesis of Mitochondrial Proteins. *Trends Biochem. Sci.* **45**, 650-667. doi:10.1016/j.tibs.2020.04.001

Casson, J., McKenna, M. and High, S. (2016). On the road to nowhere: cross-talk between post-translational protein targeting and cytosolic quality control. *Biochem. Soc. Trans.* **44**, 796-801. doi:10.1042/BST20160045

Casson, J., McKenna, M., Hassdenteufel, S., Aviram, N., Zimmerman, R. and High, S. (2017). Multiple pathways facilitate the biogenesis of mammalian tail-anchored proteins. *J. Cell Sci.* **130**, 3851-3861. doi:10.1242/jcs.207829

Cichocki, B. A., Krumpe, K., Vitali, D. G. and Rapaport, D. (2018). Pex19 is involved in importing dually targeted tail-anchored proteins to both mitochondria and peroxisomes. *Traffic* **19**, 770-785. doi:10.1111/tra.12604

Costello, J. L., Castro, I. G., Camoes, F., Schrader, T. A., McNeall, D., Yang, J., Giannopoulou, E. A., Gomes, S., Pogenberg, V., Bonekamp, N. A. et al. (2017). Predicting the targeting of tail-anchored proteins to subcellular compartments in mammalian cells. *J. Cell Sci.* **130**, 1675-1687. doi:10.1242/jcs.200204

Coy-Vergara, J., Rivera-Monroy, J., Urlaub, H., Lenz, C. and Schwappach, B. (2019). A trap mutant reveals the physiological client spectrum of TRC40. *J. Cell Sci.* **132**, jcs230094. doi:10.1242/jcs.230094

Cross, B. C. S., Sinning, I., Luirink, J. and High, S. (2009). Delivering proteins for export from the cytosol. *Nat. Rev. Mol. Cell Biol.* **10**, 255-264. doi:10.1038/nrm2657

Dixit, E., Boulant, S., Zhang, Y., Lee, A. S. Y., Odendall, C., Shum, B., Hacohen, N., Chen, Z. J., Whelan, S. P., Fransen, M. et al. (2010). Peroxisomes are signaling platforms for antiviral innate immunity. *Cell* **141**, 668-681. doi:10.1016/j.cell.2010.04.018

Esser-Nobis, K., Hatfield, L. D. and Gale, M.Jr. (2020). Spatiotemporal dynamics of innate immune signaling via RIG-I-like receptors. *Proc. Natl. Acad. Sci. USA* **117**, 15778-15788. doi:10.1073/pnas.1921861117

Farkas, A. and Bohnsack, K. E. (2021). Capture and delivery of tail-anchored proteins to the endoplasmic reticulum. *J. Cell Biol.* **220**, e202105004. doi:10.1083/jcb.202105004

Guna, A., Volkmar, N., Christianson, J. C. and Hegde, R. S. (2018). The ER membrane protein complex is a transmembrane domain insertase. *Science* **359**, 470-473. doi:10.1126/science.aao3099

Hansen, K. G., Aviram, N., Laborenz, J., Bibi, C., Meyer, M., Spang, A., Schuldiner, M. and Herrmann, J. M. (2018). An ER surface retrieval pathway safeguards the import of mitochondrial membrane proteins in yeast. *Science* **361**, 1118-1122. doi:10.1126/science.aar8174

Hassdenteufel, S., Sicking, M., Schorr, S., Aviram, N., Fecher-Trost, C., Schuldiner, M., Jung, M., Zimmermann, R. and Lang, S. (2017). hSnd2 protein represents an alternative targeting factor to the endoplasmic reticulum in human cells. *FEBS Lett.* **591**, 3211-3224. doi:10.1002/1873-3468.12831

Hegde, R. S. and Keenan, R. J. (2021). The mechanisms of integral membrane protein biogenesis. *Nat. Rev. Mol. Cell Biol.* **23**, 107-124. doi:10.1038/s41580-021-00413-2

Hessa, T., Sharma, A., Mariappan, M., Eshleman, H. D., Gutierrez, E. and Hegde, R. S. (2011). Protein targeting and degradation are coupled for elimination of mislocalized proteins. *Nature* **475**, 394-397. doi:10.1038/nature10181

Horner, S. M., Liu, H. M., Park, H. S., Briley, J. and Gale, M.Jr. (2011). Mitochondrial-associated endoplasmic reticulum membranes (MAM) form innate immune synapses and are targeted by hepatitis C virus. *Proc. Natl. Acad. Sci. USA* **108**, 14590-14595. doi:10.1073/pnas.1110133108

Itakura, E., Zavodszky, E., Shao, S., Wohlever, M. L., Keenan, R. J. and Hegde, R. S. (2016). Ubiquilins chaperone and triage mitochondrial membrane proteins for degradation. *Mol. Cell* **63**, 21-33. doi:10.1016/j.molcel.2016.05.020

Johnson, N., Powis, K. and High, S. (2013). Post-translational translocation into the endoplasmic reticulum. *Biochim. Biophys. Acta* **1833**, 2403-2409. doi:10.1016/j.bbamcr.2012.12.008

Jonikas, M. C., Collins, S. R., Denic, V., Oh, E., Quan, E. M., Schmid, V., Weibezahn, J., Schwappach, B., Walter, P., Weissman, J. S. et al. (2009). Comprehensive characterization of genes required for protein folding in the endoplasmic reticulum. *Science* **323**, 1693-1697. doi:10.1126/science.1167983

Kato, H., Takeuchi, O., Mikamo-Satoh, E., Hirai, R., Kawai, T., Matsushita, K., Hiiragi, A., Dermody, T. S., Fujita, T. and Akira, S. (2008). Length-dependent recognition of double-stranded ribonucleic acids by retinoic acid-inducible gene-I and melanoma differentiation-associated gene 5. *J. Exp. Med.* **205**, 1601-1610. doi:10.1084/jem.20080091

Kim, D. I., Jensen, S. C., Noble, K. A., Kc, B., Roux, K. H., Motamedchaboki, K. and Roux, K. J. (2016). An improved smaller biotin ligase for BioID proximity labeling. *Mol. Biol. Cell* **27**, 1188-1196. doi:10.1091/mbc.E15-12-0844

Koch, C., Schuldiner, M. and Herrmann, J. M. (2021). ER-SURF: riding the endoplasmic reticulum surface to mitochondria. *Int. J. Mol. Sci.* **22**, 9655. doi:10.3390/ijms22179655

Krumpe, K., Frumkin, I., Herzig, Y., Rimon, N., Özbalci, C., Brügger, B., Rapaport, D. and Schuldiner, M. (2012). Ergosterol content specifies targeting of tail-anchored proteins to mitochondrial outer membranes. *Mol. Biol. Cell* **23**, 3927-3935. doi:10.1091/mbc.e11-12-0994

Krysztofinska, E. M., Martínez-Lumbreras, S., Thapaliya, A., Evans, N. J., High, S. and Isaacson, R. L. (2016). Structural and functional insights into the E3 ligase, RNF126. *Sci. Rep.* **6**, 26433. doi:10.1038/srep26433

Kutay, U., Hartmann, E. and Rapoport, T. A. (1993). A class of membrane proteins with a C-terminal anchor. *Trends Cell Biol.* **3**, 72-75. doi:10.1016/0962-8924(93)90066-A

Leznicki, P. and High, S. (2012). SGTA antagonizes BAG6-mediated protein triage. *Proc. Natl. Acad. Sci. USA* **109**, 19214-19219. doi:10.1073/pnas.1209997109

Leznicki, P. and High, S. (2020). SGTA associates with nascent membrane protein precursors. *EMBO Rep.* **21**, e48835. doi:10.15252/embr.201948835

Leznicki, P., Clancy, A., Schwappach, B. and High, S. (2010). Bat3 promotes the membrane integration of tail-anchored proteins. *J. Cell Sci.* **123**, 2170-2178. doi:10.1242/jcs.066738

Leznicki, P., Roebuck, Q. P., Wunderley, L., Clancy, A., Krysztofinska, E. M., Isaacson, R. L., Warwicker, J., Schwappach, B. and High, S. (2013). The association of BAG6 with SGTA and tail-anchored proteins. *PLoS ONE* **8**, e59590. doi:10.1371/journal.pone.0059590

Leznicki, P., Korac-Prlic, J., Kliza, K., Husnjak, K., Nyathi, Y., Dikic, I. and High, S. (2015). Binding of SGTA to Rpn13 selectively modulates protein quality control. *J. Cell Sci.* **128**, 3187-3196. doi:10.1242/jcs.165209

Li, S., Wang, L., Berman, M., Kong, Y.-Y. and Dorf, M. E. (2011). Mapping a dynamic innate immunity protein interaction network regulating type I interferon production. *Immunity* **35**, 426-440. doi:10.1016/j.immuni.2011.06.014

Lin, K.-F., Fry, M. Y., Saladi, S. M. and Clemons, W. M.Jr. (2021). Molecular basis of tail-anchored integral membrane protein recognition by the cochaperone Sgt2. *J. Biol. Chem.* **296**, 100441. doi:10.1016/j.jbc.2021.100441

Liou, S.-T. and Wang, C. (2005). Small glutamine-rich tetratricopeptide repeat-containing protein is composed of three structural units with distinct functions. *Arch. Biochem. Biophys.* **435**, 253-263. doi:10.1016/j.abb.2004.12.020

Martínez-Lumbreras, S., Krysztofinska, E. M., Thapaliya, A., Spilotros, A., Matak-Vinkovic, D., Salvadori, E., Roboti, P., Nyathi, Y., Muench, J. H., Roessler, M. M. et al. (2018). Structural complexity of the co-chaperone SGTA: a conserved C-terminal region is implicated in dimerization and substrate quality control. *BMC Biol.* **16**, 76. doi:10.1186/s12915-018-0542-3

Mayerhofer, P. U. (2016). Targeting and insertion of peroxisomal membrane proteins: ER trafficking versus direct delivery to peroxisomes. *Biochim. Biophys. Acta* **1863**, 870-880. doi:10.1016/j.bbamcr.2015.09.021

McDowell, M. A., Heimes, M., Fiorentino, F., Mehmood, S., Farkas, A., Coy-Vergara, J., Wu, D., Bolla, J. R., Schmid, V., Heinze, R. et al. (2020). Structural basis of tail-anchored membrane protein biogenesis by the GET insertase complex. *Mol. Cell* **80**, 72-86.e7. doi:10.1016/j.molcel.2020.08.012

McKenna, M. J., Sim, S. I., Ordureau, A., Wei, L., Harper, J. W., Shao, S. and Park, E. (2020). The endoplasmic reticulum P5A-ATPase is a transmembrane helix dislocase. *Science* **369**, eabc5809. doi:10.1126/science.abc5809

Minami, R., Hayakawa, A., Kagawa, H., Yanagi, Y., Yokosawa, H. and Kawahara, H. (2010). BAG-6 is essential for selective elimination of defective proteasomal substrates. *J. Cell Biol.* **190**, 637-650. doi:10.1083/jcb.200908092

Mock, J.-Y., Chartron, J. W., Zaslaver, M., Xu, Y., Ye, Y. and Clemons, W. M.Jr. (2015). Bag6 complex contains a minimal tail-anchor-targeting module and a mock BAG domain. *Proc. Natl. Acad. Sci. USA* **112**, 106-111. doi:10.1073/pnas.1402745112

Norlin, S., Parekh, V. S., Naredi, P. and Edlund, H. (2016). Asna1/TRC40 controls β-cell function and endoplasmic reticulum homeostasis by ensuring retrograde transport. *Diabetes* **65**, 110-119. doi:10.2337/db15-0699

O'Keefe, S., Pool, M. R. and High, S. (2021a). Membrane protein biogenesis at the ER: the highways and byways. *FEBS J.* doi:10.1111/febs.15905

O'Keefe, S., Zong, G., Duah, K. B., Andrews, L. E., Shi, W. Q. and High, S. (2021b). An alternative pathway for membrane protein biogenesis at the endoplasmic reticulum. *Commun. Biol.* **4**, 828. doi:10.1038/s42003-021-02363-z

Payapilly, A. and High, S. (2014). BAG6 regulates the quality control of a polytopic ERAD substrate. *J. Cell Sci.* **127**, 2898-2909. doi:10.1242/jcs.145565

Perez-Riverol, Y., Csordas, A., Bai, J., Bernal-Llinares, M., Hewapathirana, S., Kundu, D. J., Inuganti, A., Griss, J., Mayer, G., Eisenacher, M. et al. (2019). The PRIDE database and related tools and resources in 2019: improving support for quantification data. *Nucleic Acids Res.* **47**, D442-D450. doi:10.1093/nar/gky1106

Pfaff, J., Rivera Monroy, J., Jamieson, C., Rajanala, K., Vilardi, F., Schwappach, B. and Kehlenbach, R. H. (2016). Emery-Dreifuss muscular dystrophy mutations impair TRC40-mediated targeting of emerin to the inner nuclear membrane. *J. Cell Sci.* **129**, 502-516. doi:10.1242/jcs.179333

Pourhaghighi, R., Ash, P. E. A., Phanse, S., Goebels, F., Hu, L. Z. M., Chen, S., Zhang, Y., Wierbowski, S. D., Boudeau, S., Moutaoufik, M. T. et al. (2020). BraInMap elucidates the macromolecular connectivity landscape of mammalian brain. *Cell Syst.* **10**, 333-350.e14. doi:10.1016/j.cels.2020.03.003

Ran, F. A., Hsu, P. D., Wright, J., Agarwala, V., Scott, D. A. and Zhang, F. (2013). Genome engineering using the CRISPR-Cas9 system. *Nat. Protoc.* **8**, 2281-2308. doi:10.1038/nprot.2013.143

Rao, M., Okreglak, V., Chio, U. S., Cho, H., Walter, P. and Shan, S.-O. (2016). Multiple selection filters ensure accurate tail-anchored membrane protein targeting. *eLife* **5**, e21301. doi:10.7554/eLife.21301

Ren, Z., Ding, T., Zuo, Z., Xu, Z., Deng, J. and Wei, Z. (2020). Regulation of MAVS expression and signaling function in the antiviral innate immune response. *Front. Immunol.* **11**, 1030. doi:10.3389/fimmu.2020.01030

Rivera-Monroy, J., Musiol, L., Unthan-Fechner, K., Farkas, A., Clancy, A., Coy-Vergara, J., Weill, U., Gockel, S., Lin, S.-Y., Corey, D. P. et al. (2016). Mice lacking WRB reveal differential biogenesis requirements of tail-anchored proteins in vivo. *Sci. Rep.* **6**, 39464. doi:10.1038/srep39464

Roberts, J. D., Thapaliya, A., Martínez-Lumbreras, S., Krysztofinska, E. M. and Isaacson, R. L. (2015). Structural and functional insights into small, glutamine-rich, tetratricopeptide repeat protein alpha. *Front. Mol. Biosci.* **2**, 71. doi:10.3389/fmolb.2015.00071

Roboti, P. and High, S. (2012). The oligosaccharyltransferase subunits OST48, DAD1 and KCP2 function as ubiquitous and selective modulators of mammalian N-glycosylation. *J. Cell Sci.* **125**, 3474-3484. doi:10.1242/jcs.103952

Roboti, P., Witkos, T. M. and Lowe, M. (2013). Biochemical analysis of secretory trafficking in mammalian cells. *Methods Cell Biol.* **118**, 85-103. doi:10.1016/B978-0-12-417164-0.00006-9

Rodrigo-Brenni, M. C., Gutierrez, E. and Hegde, R. S. (2014). Cytosolic quality control of mislocalized proteins requires RNF126 recruitment to Bag6. *Mol. Cell* **55**, 227-237. doi:10.1016/j.molcel.2014.05.025

Schrul, B. and Kopito, R. R. (2016). Peroxin-dependent targeting of a lipid-droplet-destined membrane protein to ER subdomains. *Nat. Cell Biol.* **18**, 740-751. doi:10.1038/ncb3373

Schuldiner, M., Metz, J., Schmid, V., Denic, V., Rakwalska, M., Schmitt, H. D., Schwappach, B. and Weissman, J. S. (2008). The GET complex mediates insertion of tail-anchored proteins into the ER membrane. *Cell* **134**, 634-645. doi:10.1016/j.cell.2008.06.025

Seth, R. B., Sun, L., Ea, C.-K. and Chen, Z. J. (2005). Identification and characterization of MAVS, a mitochondrial antiviral signaling protein that activates NF-κB and IRF3. *Cell* **122**, 669-682. doi:10.1016/j.cell.2005.08.012

Shao, S., Rodrigo-Brenni, M. C., Kivlen, M. H. and Hegde, R. S. (2017). Mechanistic basis for a molecular triage reaction. *Science* **355**, 298-302. doi:10.1126/science.aah6130

Suzuki, R. and Kawahara, H. (2016). UBQLN4 recognizes mislocalized transmembrane domain proteins and targets these to proteasomal degradation. *EMBO Rep.* **17**, 842-857. doi:10.15252/embr.201541402

Teo, G., Liu, G., Zhang, J., Nesvizhskii, A. I., Gingras, A.-C. and Choi, H. (2014). SAINTexpress: improvements and additional features in Significance Analysis of INTeractome software. *J. Proteomics* **100**, 37-43. doi:10.1016/j.jprot.2013.10.023

Thoresen, D., Wang, W., Galls, D., Guo, R., Xu, L. and Pyle, A. M. (2021). The molecular mechanism of RIG-I activation and signaling. *Immunol. Rev.* **304**, 154-168. doi:10.1111/imr.13022

Vazquez, C. and Horner, S. M. (2015). MAVS coordination of antiviral innate immunity. *J. Virol.* **89**, 6974-6977. doi:10.1128/JVI.01918-14

Vogl, C., Panou, I., Yamanbaeva, G., Wichmann, C., Mangosing, S. J., Vilardi, F., Indzhykulian, A. A., Pangršič, T., Santarelli, R., Rodriguez-Ballesteros, M. et al. (2016). Tryptophan-rich basic protein (WRB) mediates insertion of the tail-anchored protein otoferlin and is required for hair cell exocytosis and hearing. *EMBO J.* **35**, 2536-2552. doi:10.15252/embj.201593565

Walczak, C. P., Ravindran, M. S., Inoue, T. and Tsai, B. (2014). A cytosolic chaperone complexes with dynamic membrane J-proteins and mobilizes a nonenveloped virus out of the endoplasmic reticulum. *PLoS Pathog.* **10**, e1004007. doi:10.1371/journal.ppat.1004007

Wang, F., Brown, E. C., Mak, G., Zhuang, J. and Denic, V. (2010). A chaperone cascade sorts proteins for posttranslational membrane insertion into the endoplasmic reticulum. *Mol. Cell* **40**, 159-171. doi:10.1016/j.molcel.2010.08.038

Wang, Q., Liu, Y., Soetandyo, N., Baek, K., Hegde, R. and Ye, Y. (2011). A ubiquitin ligase-associated chaperone holdase maintains polypeptides in soluble states for proteasome degradation. *Mol. Cell* **42**, 758-770. doi:10.1016/j.molcel.2011.05.010

Winnefeld, M., Grewenig, A., Schnölzer, M., Spring, H., Knoch, T. A., Gan, E. C., Rommelaere, J. and Cziepluch, C. (2006). Human SGT interacts with Bag-6/Bat-3/Scythe and cells with reduced levels of either protein display persistence of few misaligned chromosomes and mitotic arrest. *Exp. Cell Res.* **312**, 2500-2514. doi:10.1016/j.yexcr.2006.04.020

Wu, H., Carvalho, P. and Voeltz, G. K. (2018). Here, there, and everywhere: the importance of ER membrane contact sites. *Science* **361**, eaan5835. doi:10.1126/science.aan5835

Wunderley, L., Leznicki, P., Payapilly, A. and High, S. (2014). SGTA regulates the cytosolic quality control of hydrophobic substrates. *J. Cell Sci.* **127**, 4728-4739. doi:10.1242/jcs.155648

Xu, Y., Cai, M., Yang, Y., Huang, L. and Ye, Y. (2012). SGTA recognizes a noncanonical ubiquitin-like domain in the Bag6-Ubl4A-Trc35 complex to promote endoplasmic reticulum-associated degradation. *Cell Rep.* **2**, 1633-1644. doi:10.1016/j.celrep.2012.11.010

Yamamoto, K., Hayashishita, M., Minami, S., Suzuki, K., Hagiwara, T., Noguchi, A. and Kawahara, H. (2017). Elimination of a signal sequence-uncleaved form of defective HLA protein through BAG6. *Sci. Rep.* **7**, 14545. doi:10.1038/s41598-017-14975-9

Figure S1
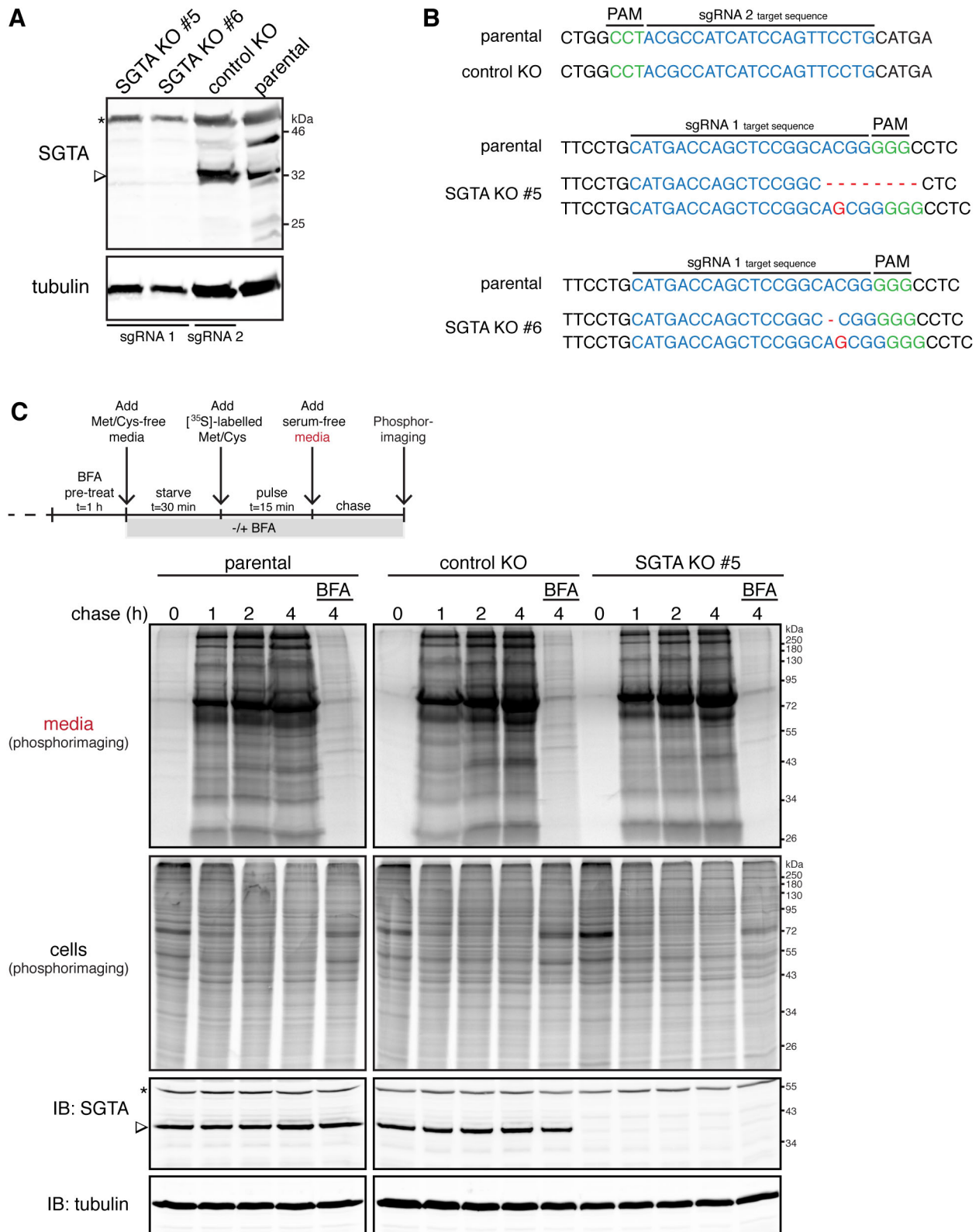
Fig. S1. Confirmation of SGTA KO in HepG2 cells. CRISPR-Cas9-mediated disruption of exon 2 of the SGTA gene in HepG2 cells resulted in a loss of SGTA. For the generation of SGTA KO cells, we designed single guide RNAs (sgRNAs) targeting the exon 2 of human SGTA (see Materials and Methods), which is present in all putative SGTA isoforms (Ensemble accession ENSG00000104969). SGTA KO clonal cell lines #5 (used hereafter) and #6 were obtained using sgRNA 1. Control KO cells are clones that underwent the same manipulation with SGTA KO cells using sgRNA 2, but retained SGTA expression. (A) Total lysates from parental, control KO and SGTA KO HepG2 cells were analysed by immunoblotting with anti-SGTA and anti-tubulin antibodies. The SGTA signal is marked by an arrowhead, while a non-specific band retained in SGTA KO cells is indicated by an asterisk. (B) Sequence alignment of partial SGTA coding sequences from parental and control KO/SGTA KO HepG2 cells. PAM (protospacer adjacent motif), green; sgRNA target sequence, blue; mutated sequence, red. (C) SGTA deficiency does not inhibit global protein secretion. HepG2 cells were left untreated or treated with brefeldin A (BFA; 2.5 μg/ml) for 1 h. Newly synthesised proteins were pulse-labelled for 15 min and then chased in serum-free medium containing unlabelled Met and Cys for various times in the absence or presence of BFA, as shown in the schematic representation of the assay. At the end of the chase, radiolabelled proteins in media (upper panel) and whole cell lysates (bottom panel) were resolved by SDS-PAGE and visualised by phosphorimaging. Whole cell lysates were also analysed by immunoblotting (IB) with anti-SGTA and anti-tubulin antibodies. The arrowhead points to the SGTA signal and the asterisk indicates a non-specific band.

Figure S2
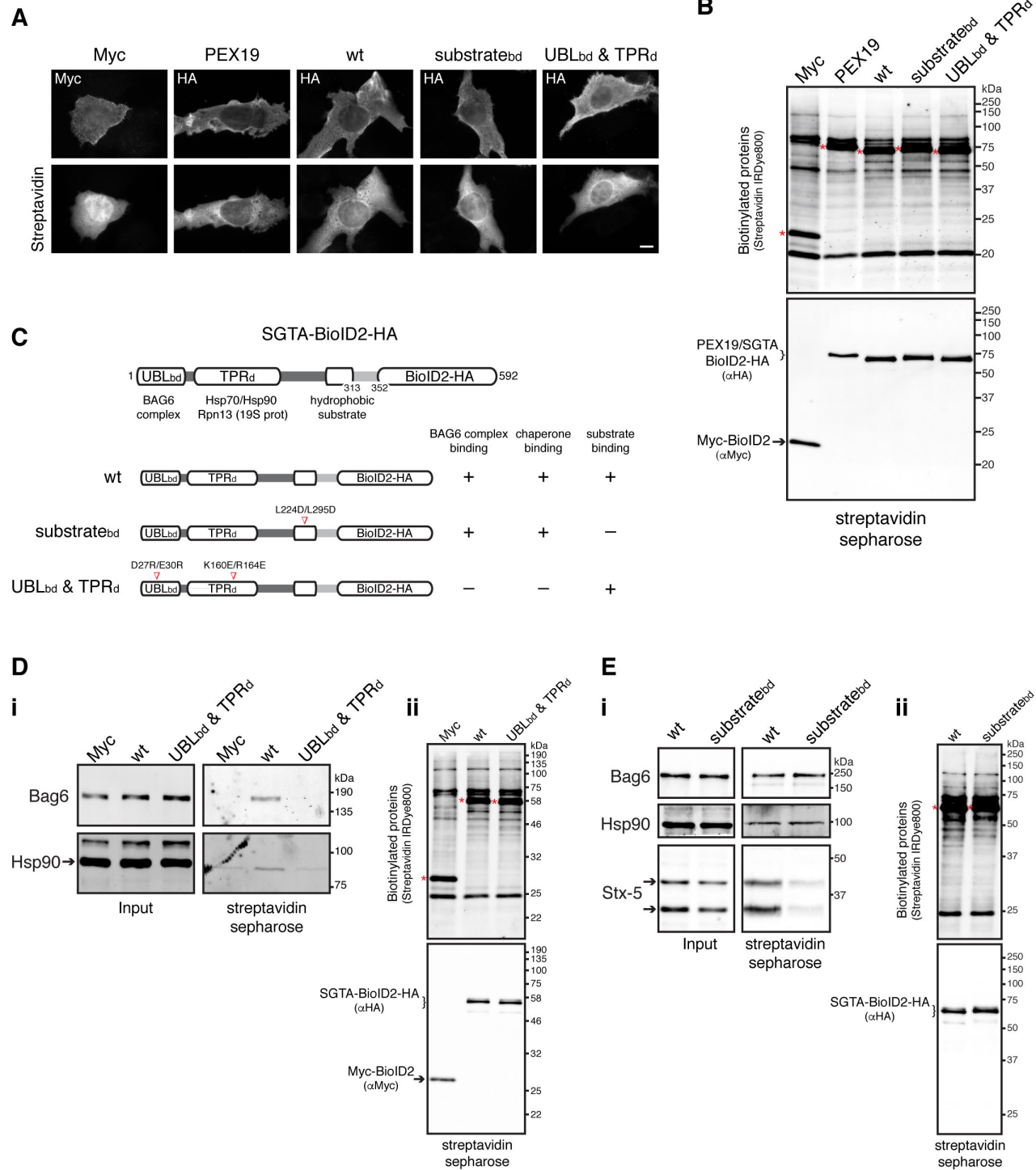
Fig. S2. Validation of BioID2-based assay for proximity labelling of SGTA proteome. (A,B) Demonstration of the cytosolic localisation and the biotinylation activity of bait-BioID2 fusion proteins. SGTA KO cells transiently transfected with plasmids encoding Myc-BioID2, PEX19-BioID2 or the indicated SGTA-BioID2 variants were incubated with exogenous biotin for 8 h. (A) Cells were fixed and stained with anti-Myc/anti-HA and fluorophore-conjugated streptavidin to visualise BioID2-tagged baits and biotinylated proteins, respectively. Representative wide-field fluorescence images are shown. Scale bar, 10 μm. (B) Cells were lysed and biotinylated proteins were isolated on streptavidin sepharose beads. The streptavidin-bound material was eluted using a biotin-containing buffer, resolved by SDS-PAGE and immunoblotted for BioID2-tagged baits (anti-Myc/anti-HA) or probed with streptavidin to detect total biotinylated proteins in each sample. The signals from self-biotinylated BioID2-tagged baits were detected at the predicted molecular weights and are marked with red asterisks. (C-E) Detection of known SGTA interactors by a small-scale streptavidin pull-down assay. SGTA KO cells transiently expressing the indicated BioID2-tagged baits (see schematic in C; also shown in Fig. 1A) were treated with biotin for 8 h. (Di,Ei) Whole cell lysates (Input) and biotinylated proteins (streptavidin sepharose) were analysed by immunoblotting for the indicated endogenous proteins. Note that samples were analysed on two different gels and the combined image was produced using the same brightness and contrast settings. (Dii,Eii) Biotinylated proteins (streptavidin sepharose) were analysed by immunoblotting for BioID2-tagged baits (anti-Myc/anti-HA) and total biotinylated proteins (Streptavidin IRDye800). The signals from self-biotinylated BioID2-tagged baits are marked with red asterisks. Syntaxin-5 (Stx-5) appears as two bands (hereafter indicated by arrows) corresponding to two isoforms, a 42 kDa-ER and a 35 kDa-Golgi isoform that result from an alternative initiation of translation (Coy-Vergara et al., 2019).
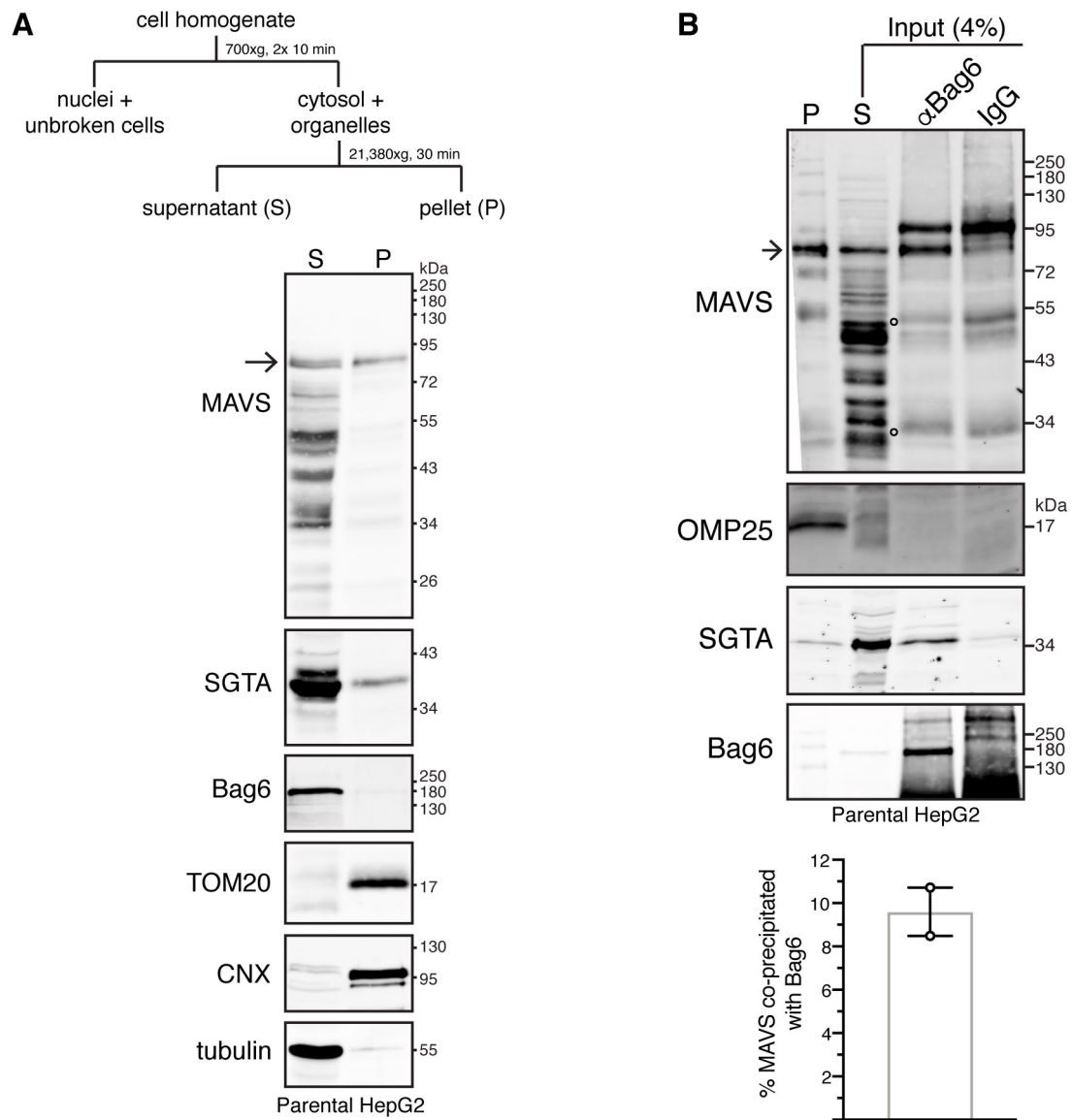
Figure S3
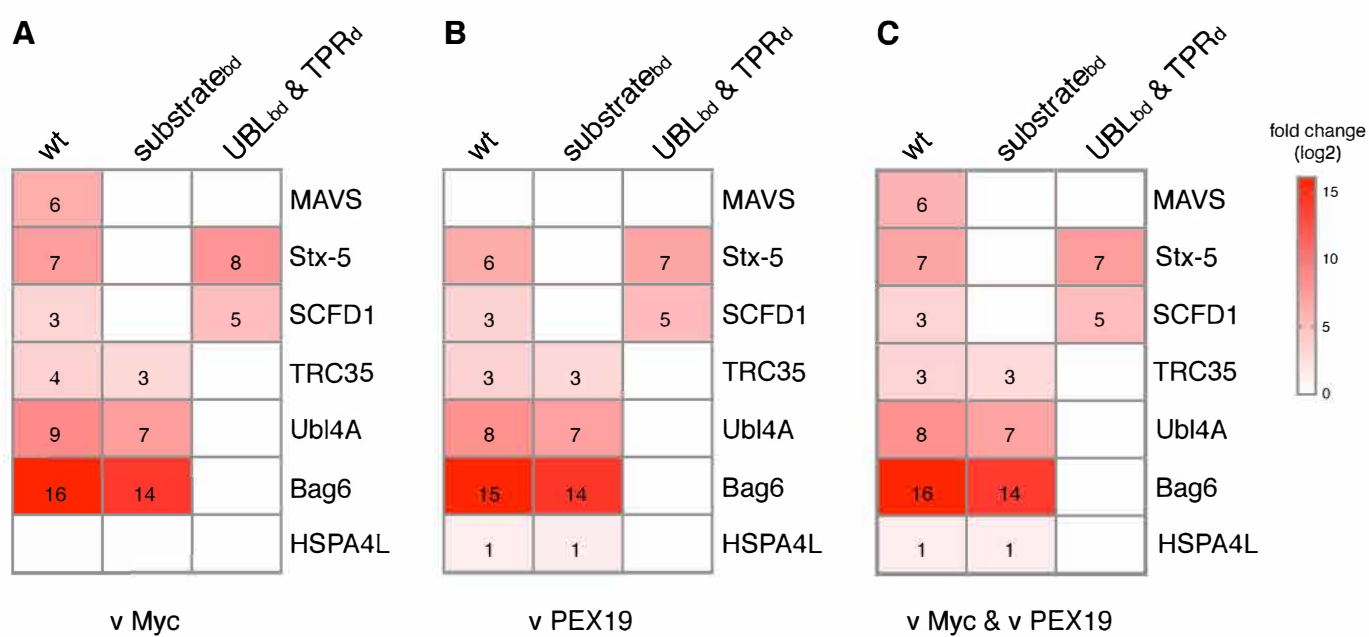
Fig. S3. Profiling of SGTA interactors by proximity-labelling proteomics. Heat maps representing log2-transformed fold changes in the protein intensities of high-confidence (BFDR<0.05) wild-type (wt)/mutant SGTA-specific preys relative to (A) Myc-BioID2, (B) PEX19-BioID2 and (C) both Myc-BioID2 and PEX19-BioID2 controls. Individual rounded values are depicted in the heat maps. A non-significant prey is shown as a white box (three biological replicates, see Tables S1-S3 for list of all the detected proteins).

Figure S4

A

cell homogenate

700xg, 2x 10 min

nuclei + unbroken cells

cytosol + organelles

21,380xg, 30 min

supernatant (S)   pellet (P)

Parental HepG2

B

Input (4%)

Parental HepG2

C

TA protein

TMD   CTE

TA protein	TMD	CTE	Predicted hydropathy	Predicted α-helicity	Destination membrane
MAVS	GALWLQVAVTGVLVVTLLVVL	YRRRLH	2.34	0.18	MOM / Peroxisomes
OMP25	IPIFMVLVPVFALTMVAAWAF	MRYRQQL	2.29	0.56	MOM
Stx-5	WLMVKIFLILIVFFIIFVVFL	A	3.12	4.58	ER

Fig. S4. Bag6-MAVS interaction in parental HepG2 cells. (A) Top: Schematic of the subcellular fractionation protocol used to separate the cell homogenate into crude cytosolic supernatant (S) and membrane-associated pellet (P) fractions. Bottom: Detergent-free extracts from parental HepG2 cells were fractionated as shown above. Equivalent amounts of each fraction were analysed by immunoblotting for MAVS and various compartmental markers. Bag6, SGTA and tubulin (cytosolic markers), TOM20 (mitochondrial outer membrane marker) and Calnexin (CNX, ER membrane marker) serve as fractionation controls. Full-length MAVS species (hereafter marked by an arrow) can be observed in both the cytosolic and membrane-associated fractions at steady-state (see also Fig. 2A). (B) MAVS, but not OMP25, co-immunoprecipitates with Bag6. The supernatant fraction from (A) was subjected to immunoprecipitations with equal amounts of rabbit anti-Bag6 antibody or rabbit IgG antibody (control for non-specific binding). Equivalent amounts of pellet (P) and supernatant (S) fractions from (A) and immunoprecipitates were analysed by immunoblotting for the indicated endogenous proteins. SGTA served as a positive control for Bag6 binding. Open circles on MAVS blot indicate signals derived from denatured antibody heavy and light chains. In contrast to full-length MAVS that is distributed in both fractions, OMP25 is predominantly present in the membrane-associated pellet fraction. The levels of MAVS that co-immunoprecipitate with Bag6 were reported as mean ± s.e.m. for two independent experiments. (C) Sequences and properties of the transmembrane domains (TMDs) and C-terminal elements (CTEs) of the TA substrates used in this study. Sequences of TMDs were obtained from UniProt. For predicted hydropathy, Grand Average of Hydropathy (GRAVY) scores were calculated (http://www.gravy-calculator.de). For predicted α-helicity, scores (% helical content) was calculated at pH 7.0, 310.15 K, ionic strength 0.13 M using the Agadir prediction algorithm (http://agadir.crg.es) (Munoz and Serrano, 1997). MOM, mitochondrial outer membrane; ER, endoplasmic reticulum.

Figure S5

control KO HepG2
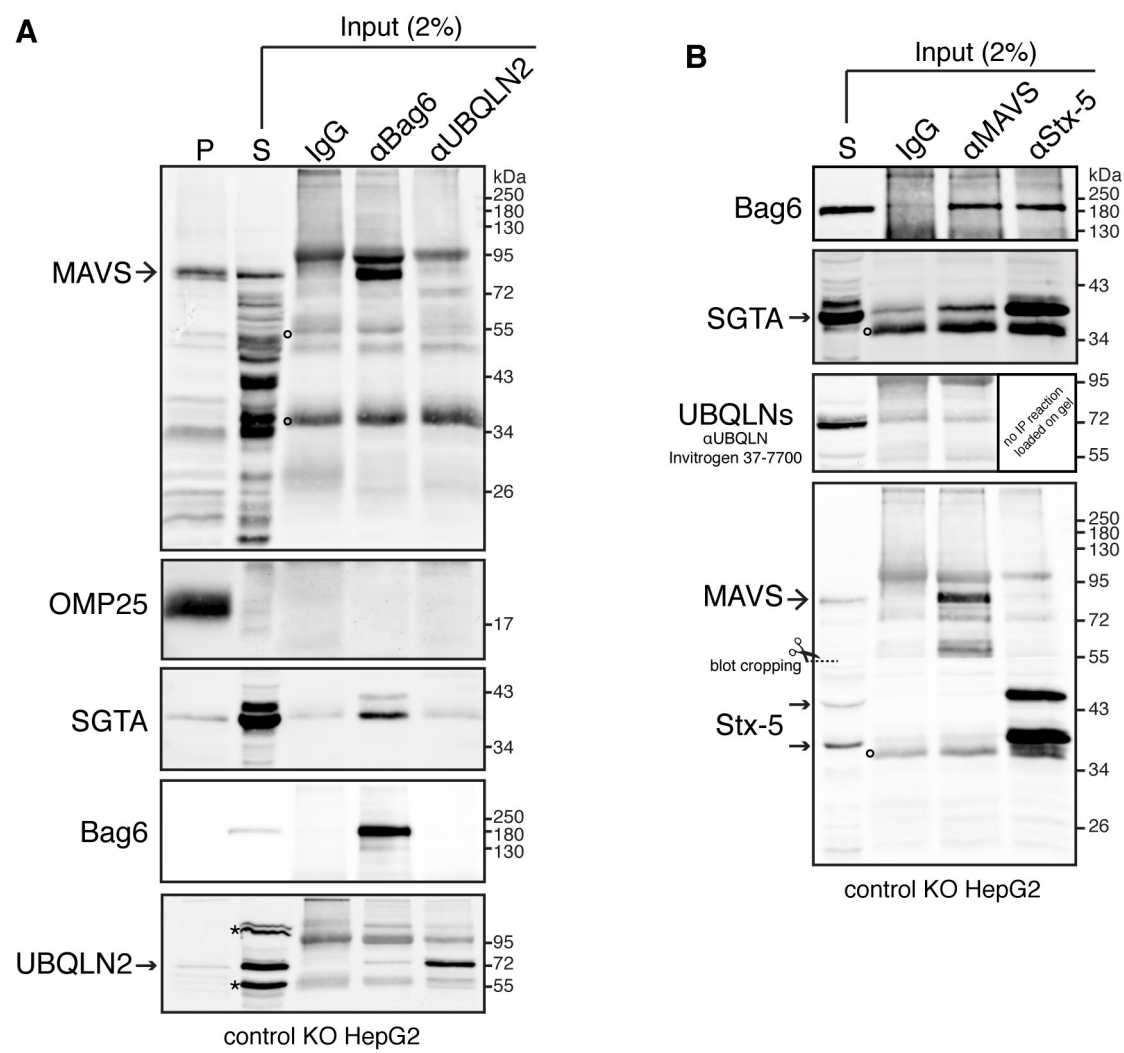
Fig. S5. No association of MAVS with Ubiquilins can be detected by co-immunoprecipitation studies. (A) MAVS does not co-immunoprecipitate with Ubiquilin-2 (UBQLN2). Control KO cells were fractionated as shown in the schematic of Fig. S4A and the supernatant fraction was subjected to immunoprecipitations with equal amounts of rabbit anti-Bag6, rabbit anti-UBQLN2 or rabbit IgG (control for non-specific binding) antibodies. Equivalent amounts of pellet (P) and supernatant (S) fractions and immunoprecipitates were analysed by immunoblotting for the indicated endogenous proteins. SGTA served as positive control for Bag6 binding. Asterisks indicate non-specific products. (B) Ubiquilins (UBQLNs) do not co-immunoprecipitate with MAVS. Control KO cells were fractionated as shown in the schematic of Fig. S4A and the supernatant (S) fraction was subjected to immunoprecipitations with equal amounts of rabbit anti-MAVS, rabbit anti-Stx-5 or rabbit IgG (control for non-specific binding) antibodies. Input and immunoprecipitates were analysed by immunoblotting for the indicated endogenous proteins. Note that the Invitrogen 37-7700 anti-UBQLN antibody recognises human UBQLN-1, -2 and -4 (Safren et al., 2015). In (A) and (B), open circles indicate signals derived from denatured antibody heavy and light chains.

Figure S6

A

B

C
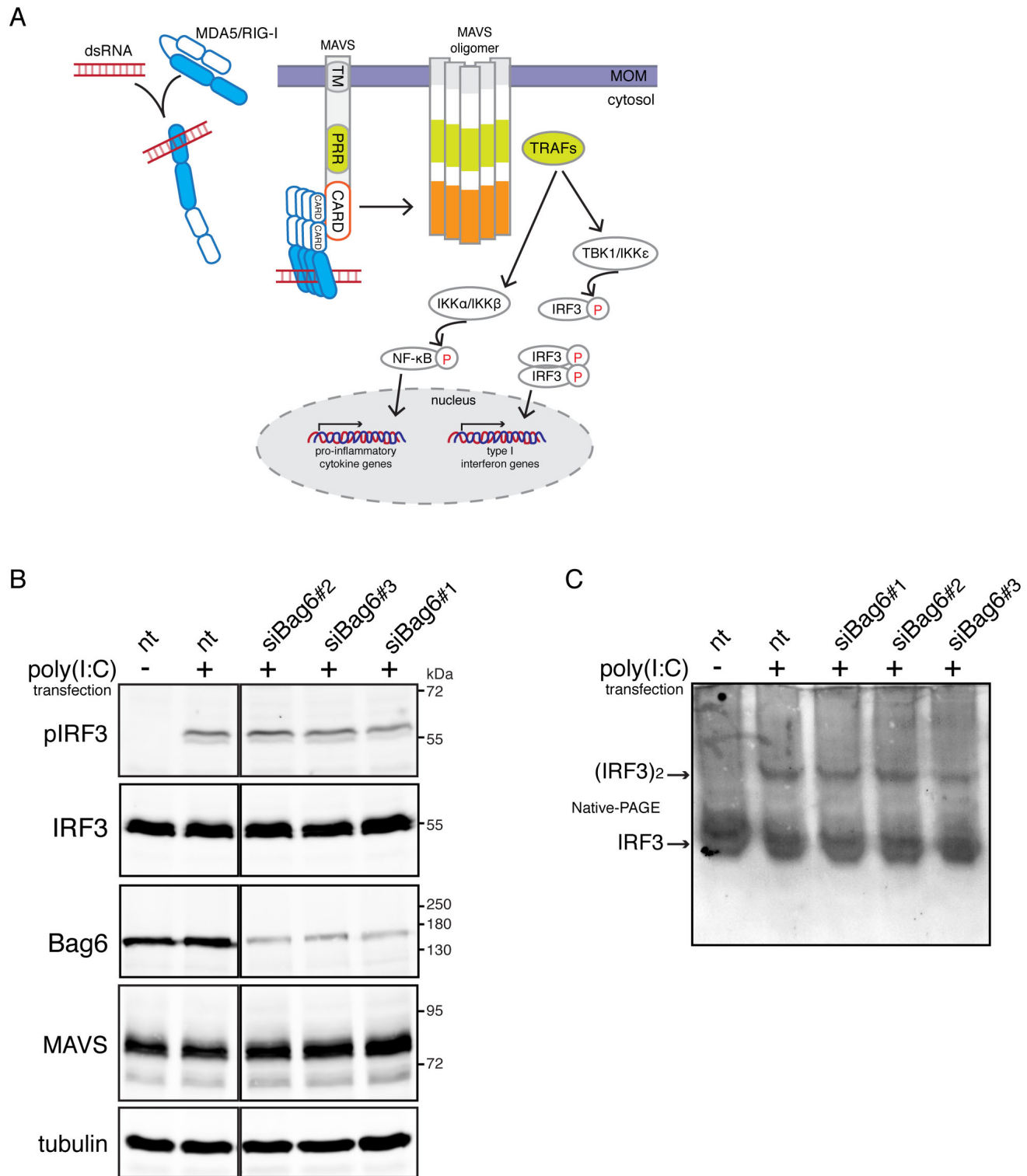
Fig. S6. Bag6 does not modulate poly(I:C)-induced MAVS-dependent signalling. (A) Schematic of RIG-I-like receptor (RLR)-dependent signalling pathway. Cytosolic double-stranded viral RNA is initially sensed by the host cell's RLRs (RIG-I and MDA5). Upon binding to the viral RNA, RLRs undergo a conformational change that exposes their caspase activation and recruitment domains (CARDs) for interactions with downstream signalling proteins. Modification of CARDs with K63 polyubiquitin chains results in the oligomerisation and activation of RLRs. Activated RLRs are recruited to the mitochondria outer membrane, where they interact with MAVS via their CARDs (Hou et al., 2011). This interaction as well as K63-linked polyubiquitination of MAVS (Liu et al., 2017) induces a conformational change leading to the formation of functional prion-like MAVS aggregates and activation of downstream signalling (Hou et al., 2011). MAVS aggregates form a signalling scaffold by recruiting and activating multiple tumour necrosis factor receptor-associated factors (TRAFs), which in turn recruit kinase complexes that phosphorylate the transcription factors IRF3 and NF-kB leading to the transcriptional upregulation of pro-inflammatory cytokines and type I interferons. (B,C) Bag6 depletion does not affect IRF3 activation in response to cytosolic poly(I:C). Control KO cells transfected with non-targeting (nt) or three independent Bag6-targeting siRNAs for 72 h were mock-treated (-) or treated with poly(I:C) (+) using typical transfection conditions (1 μg/ml, 12 h) (Li et al., 2021; Liu et al., 2017; Zhang et al., 2020) and subsequently analysed by immunoblotting for the indicated endogenous proteins. In (B), all samples were analysed on the same gel and the combined image was produced using the same brightness and contrast settings.

Figure S7
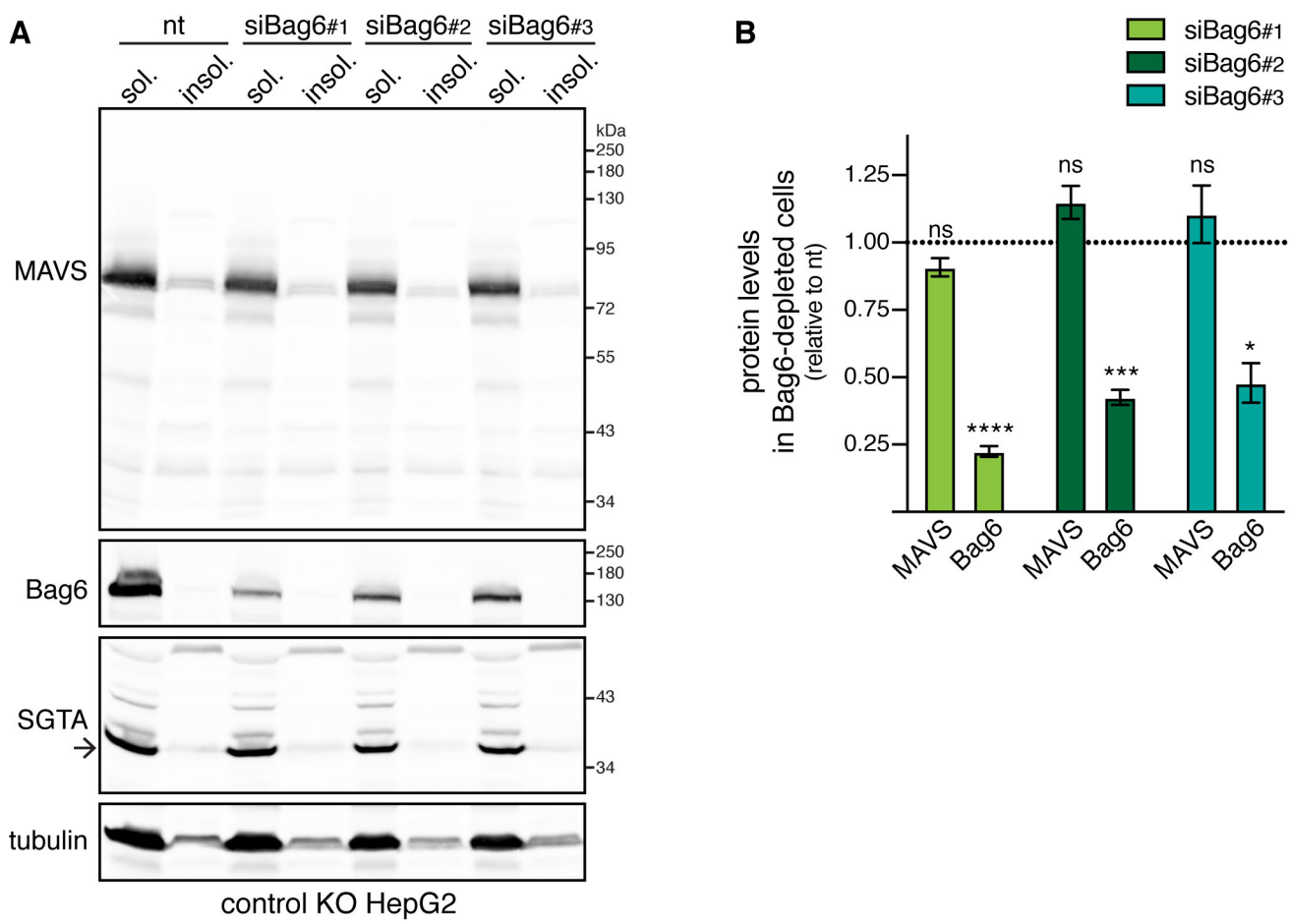
Fig. S7. Bag6 deficiency does not affect steady-state MAVS levels or solubility. (A) Control KO cells treated with non-targeting (nt) or three independent Bag6-targeting siRNAs for 72 h were harvested with a non-ionic detergent-containing lysis buffer. The resulting lysates were separated into soluble and insoluble fractions and analysed by immunoblotting for the indicated endogenous proteins. Note that endogenous MAVS appears to be uniformly soluble in Bag6-depleted cells. SGTA and tubulin remain uniformly soluble under all conditions and serve as fractionation and loading controls. (B) Bag6 and MAVS levels in siBag6-treated cells relative to nt siRNA-treated cells, where protein levels were set to 1. Shown are means ± s.e.m. for four biological replicates as shown in (A). $*P < 0.05$; $***P < 0.001$; $****P < 0.0001$; ns, not significant (one-way ANOVA with Dunnett's multiple comparison tests).

Table S1. BioID2-derived proximity interactome of SGTA_relative to both Myc-BioID2 and PEX19-BioID2 controls

Click here to download Table S1

Table S2. BioID2-derived proximity interactome of SGTA_relative to Myc-BioID2 control

Click here to download Table S2

Table S3. BioID2-derived proximity interactome of SGTA_relative to PEX19-BioID2 control

Click here to download Table S3

References

Coy-Vergara, J., Rivera-Monroy, J., Urlaub, H., Lenz, C. and Schwappach, B. (2019). A trap mutant reveals the physiological client spectrum of TRC40. *J Cell Sci* **132**, jcs230094. doi:10.1242/jcs.230094

Hou, F., Sun, L., Zheng, H., Skaug, B., Jiang, Q. X. and Chen, Z. J. (2011). MAVS forms functional prion-like aggregates to activate and propagate antiviral innate immune response. *Cell* **146**, 448-461. doi:10.1016/j.cell.2011.06.041

Li, S., Kuang, M., Chen, L., Li, Y., Liu, S., Du, H., Cao, L. and You, F. (2021). The mitochondrial protein ERAL1 suppresses RNA virus infection by facilitating RIG-I-like receptor signaling. *Cell Rep* **34**, 108631. doi:10.1016/j.celrep.2020.108631

Liu, B., Zhang, M., Chu, H., Zhang, H., Wu, H., Song, G., Wang, P., Zhao, K., Hou, J., Wang, X. et al. (2017). The ubiquitin E3 ligase TRIM31 promotes aggregation and activation of the signaling adaptor MAVS through Lys63-linked polyubiquitination. *Nat Immunol* **18**, 214-224. doi:10.1038/ni.3641

Munoz, V. and Serrano, L. (1997). Development of the multiple sequence approximation within the AGADIR model of alpha-helix formation: comparison with Zimm-Bragg and Lifson-Roig formalisms. *Biopolymers* **41**, 495-509. doi:10.1002/(SICI)1097-0282(19970415)41:5<495::AID-BIP2>3.0.CO;2-H

Safren, N., Chang, L., Dziki, K. M. and Monteiro, M. J. (2015). Signature changes in ubiquilin expression in the R6/2 mouse model of Huntington's disease. *Brain Res* **1597**, 37-46. doi:10.1016/j.brainres.2014.12.008

Zhang, Z., Fang, X., Wu, X., Ling, L., Chu, F., Li, J., Wang, S., Zang, J., Zhang, B., Ye, S. et al. (2020). Acetylation-Dependent Deubiquitinase OTUD3 Controls MAVS Activation in Innate Antiviral Immunity. *Mol Cell* **79**, 304-319 e7. doi:10.1016/j.molcel.2020.06.020